ARTICLE

A novel Hv1 inhibitor reveals a new mechanism of inhibition of a voltage-sensing domain

Chang Zhao[1,2] , Liang Hong[1], Saleh Riahi[3], Victoria T. Lim[3], Douglas J. Tobias[2,3], and Francesco Tombola[1,2]

Voltage-gated sodium, potassium, and calcium channels consist of four voltage-sensing domains (VSDs) that surround a central pore domain and transition from a down state to an up state in response to membrane depolarization. While many types of drugs bind pore domains, the number of organic molecules known to bind VSDs is limited. The Hv1 voltage-gated proton channel is made of two VSDs and does not contain a pore domain, providing a simplified model for studying how small ligands interact with VSDs. Here, we describe a ligand, named HIF, that interacts with the Hv1 VSD in the up and down states. We find that HIF rapidly inhibits proton conduction in the up state by blocking the open channel, as previously described for 2-guanidinobenzimidazole and its derivatives. HIF, however, interacts with a site slowly accessible in the down state. Functional studies and MD simulations suggest that this interaction traps the compound in a narrow pocket lined with charged residues within the VSD intracellular vestibule, which results in slow recovery from inhibition. Our findings point to a "wrench in gears" mechanism whereby side chains within the binding pocket trap the compound as the teeth of interlocking gears. We propose that the use of screening strategies designed to target binding sites with slow accessibility, similar to the one identified here, could lead to the discovery of new ligands capable of interacting with VSDs of other voltage-gated ion channels in the down state.

Introduction

The voltage-gated proton channel Hv1 plays important roles in numerous biological processes, including pH homeostasis, the immune response, and sperm cell function (DeCoursey, 2013; Lishko, 2016). It belongs to the large family of proteins containing voltage-sensing domains (VSDs), which also includes Nav, Kv, and Cav channels and voltage-sensitive phosphatases (Ramsey et al., 2006; Sasaki et al., 2006). The channel consists of two identical subunits (Koch et al., 2008; Lee et al., 2008; Tombola et al., 2008) that gate cooperatively (Gonzalez et al., 2010; Musset et al., 2010; Tombola et al., 2010). Each subunit contains four transmembrane helices, S1–S4, which form a VSD (Bayrhuber et al., 2019; Takeshita et al., 2014).

Hv1 is an emerging pharmacological target due to its role in a variety of diseases, such as ischemic stroke and cancer (Pupo and Gonzalez León, 2014; Seredenina et al., 2015). Because of its simplified structural organization, it is also a good model for studying how small molecules interact with VSDs. Proton conduction in Hv1 does not occur through a pore domain, as in other voltage-gated channels; it occurs through the VSD itself. Accordingly, ligand binding can be monitored via its direct effect on the VSD-mediated current rather than its indirect effects on

the pore domain, as first shown with the prototypical Hv1 inhibitor Zn^{2+} (Cherny and DeCoursey, 1999; DeCoursey and Cherny, 1993; Ramsey et al., 2006; Sasaki et al., 2006).

VSDs change conformation in response to membrane depolarization as their S4 helix transitions from a down state to an up state (Hille, 2001). In the Hv1 VSD, the proton conduction pathway is closed in the down state and open in the up state. The arginine-mimic 2-guanidinobenzimidazole (2GBI) was previously shown to inhibit the human Hv1 channel by binding to the intracellular side of the VSD in the open conformation (up state; Chamberlin et al., 2014; Geragotelis et al., 2020; Gianti et al., 2016; Hong et al., 2013). Both the imidazole ring and the condensed phenyl ring of the compound were found to interact with the channel (Hong et al., 2014). To improve such interactions, a new class of inhibitors was generated in which the two rings were separated by flexible linkers (Zhao et al., 2021). These compounds, including 3-(2-amino-5-methyl-1H-imidazol-4-yl)-1-(3,5-difluorophenyl)propan-1-one (HIF), were also compared with 2-aminobenzimidazole (ABI) derivatives to assess the effect of fluorination on the ligand apparent binding affinity. HIF, which contains a difluorophenyl ring, was found to be superior

---

[1]Department of Physiology and Biophysics, University of California, Irvine, Irvine, CA; [2]Chao Family Comprehensive Cancer Center, University of California, Irvine, Irvine, CA; [3]Department of Chemistry, University of California, Irvine, Irvine, CA.

Correspondence to Francesco Tombola: ftombola@uci.edu; L. Hong's present address is Department of Medicine, University of Illinois, Chicago, IL.

to both ABI and 2GBI at inhibiting Hv1, and its binding site within the VSD in the open conformation was proposed to overlap with the 2GBI binding site (Zhao et al., 2021).

Here, we investigate HIF interactions with the Hv1 VSD in more detail and find that in addition to the binding site responsible for open channel block (binding to the up state), HIF interacts with a second site that is accessible in the down state and is responsible for key features of HIF-mediated inhibition, such as the slow component of current decay and the slow recovery from inhibition. We use mutagenesis-based perturbation analysis, molecular docking, and atomistic simulations to shed light on the nature of this additional site. Its amino acid composition and structural features suggest that similar interaction sites could exist in the VSDs of other voltage-gated ion channels.

Materials and methods

DNA constructs and chemical reagents
Mutagenesis was performed as previously described (Hong et al., 2013). mRNAs were synthesized using mMESSAGE mMACHINE T7 Transcription Kit (Ambion) or HiScribe T7 ARCA mRNA Kit (with tailing; New England Biolabs) from linearized DNA constructs described in Zhao et al. (2021). All chemical reagents were at the highest purity commercially available. ABI and 2GBI were from Sigma-Aldrich. HIF, 3-(2-amino-5-methyl-1H-imidazol-4-yl)-1-phenyl-propan-1-one (HIF$_{NF}$), N-[(2-amino-5-methyl-1H-imidazol-4-yl)methyl]-3,5-difluorobenzamide (HIF$_{NH}$), 3-(2-amino-5-methyl-1H-imidazol-4-yl)-1-(3,5-difluorophenyl)propan-1-ol (HIF$_{OH}$), and (2E)-3-(2-amino-5-methyl-1H-imidazol-4-yl)-1-(3,5-difluorophenyl)prop-2-en-1-one (HIF$_{EN}$) were custom synthesized by Enamine (see Zhao et al., 2021). With the exception of HIF$_{NH}$, all HIF compounds were in the form of hydrochloride salt. Stock solutions of Hv1 inhibitors in DMSO or methanol were diluted in the bath medium at the desired final concentration before each experimental session.

Electrophysiology
Xenopus laevis oocytes were from Ecocyte Bioscience or XENOPUS1. 1–3 d before the electrophysiological measurements, cells were injected with mRNAs (50 nl/cell, 0.5–1.5 ng/nl) using a Nanoject II (Drummond Scientific). Cells were kept at 18°C in ND96 medium containing 96 mM NaCl, 2 mM KCl, 1.8 mM CaCl$_2$, 1 mM MgCl$_2$, 10 mM HEPES, 5 mM pyruvate, and 100 μg/ml gentamycin (pH 7.2). Voltage-clamp measurements were performed in inside-out patch configuration using an Axopatch 200B amplifier controlled by pClamp10 software through an Axon Digidata 1440A (Molecular Devices). The signal current was low pass filtered online at 1 kHz before digitalization (2 kHz sampling) and then further filtered offline at 150 or 200 Hz (Bessel, –80 dB/decade). All measurements were performed at 22 ± 1°C. Pipettes had 1–3 MΩ access resistance. Bath and pipette solutions contained 100 mM Mes, 30 mM TEA methanesulfonate, 5 mM TEA chloride, and 5 mM EGTA adjusted to pH 6.0 with TEA hydroxide. Unless otherwise specified, the holding potential was –40 mV, and the depolarization potential +120 mV. Channel inhibition was determined by isochronal current measurements at the end of the depolarization pulses. To test

whether the time course of HIF-mediated Hv1 inhibition was state dependent, voltage protocols with variable relative depolarization time (RDT) were used. RDT is defined as $t_d / (t_r + t_d)$, where t_d is the time spent at +120 mV and t_r the time at –40 mV between consecutive depolarizations. The $t_d / (t_r + t_d)$ values were 0.1 (2 s/20 s), 0.2 (3 s/15 s), 0.3 (3 s/10s), and 0.5 (3 s/6 s). Comparisons between HIF and its analogues and between Hv1 mutants and WT were performed at RDT = 0.2, with the exception of F150A and D112E. To properly track the fast kinetics of inhibition of Hv1 F150A, the RDT was increased to 0.3. Conversely, to properly track the slow kinetics of inhibition of Hv1 D112E, the RDT was decreased to 0.1. Matched RDTs were used for comparisons with WT. Hv1 inhibitors were introduced in the bath using a computer-controlled gravity-fed multivalve perfusion system (Warner Instruments). Fast perfusion experiments were performed with a multibarrel perfusion pencil (AutoMate Scientific) mounting a delivery tip 360 μm in diameter positioned in front of the patch pipette.

Data analysis
Clampfit 10.2 (Molecular Devices) and Origin 8.1 (OriginLab) were used for data analysis. Leak subtraction and rundown correction of current traces were performed as previously described (Hong et al., 2013). Time courses of Hv1 inhibition were fitted with the double-exponential function (Eq. 1):

$$I(t)/I_o = c_\infty + c_{fast}e^{(t_o - t)/\tau_{fast}} + c_{slow}e^{(t_o - t)/\tau_{slow}}, \quad (1)$$

where $I(t)/I_o$ is the normalized current decay in the presence of the inhibitor, and τ_{fast} and τ_{slow} are the time constants for the fast and slow components of the decay with weights c_{fast} and c_{slow}, respectively. t_o indicates the start of the decay when the perfusion of the inhibitor begins. c_∞ is the fraction of the remaining current when inhibition reaches steady state. For the recovery from inhibition, the fitting was performed with the single-exponential function (Eq. 2):

$$I(t)/I_o = 1 - c_{off}e^{(t_o - t)/\tau_{off}}, \quad (2)$$

where τ_{off} is the time constant of the recovery, while c_{off} quantifies the amplitude of the recovery. t_o indicates the time at which the inhibitor is removed from the bath compartment by perfusion of recording solution. G-V measurements were performed as the previously described (Hong et al., 2013; Tombola et al., 2010). Conductance was determined from $G(V_{test}) = (I_{test} - I_{tail}) / (V_{test} - V_{tail})$, where I_{tail} and V_{tail} are the tail current and voltage (–40 mV) following the depolarization step at V_{test} (ranging from –20 mV to +130 mV) and I_{test} the current measured at the end of the depolarization step. G_{max} was determined from maximal I_{tail} (and corresponding I_{test}) in the V_{test} region in which the tail current saturated. Current rundown was corrected using a reference depolarization step preceding the test depolarization. G-V plots were fitted with the Boltzmann equation (Eq. 3):

$$G/G_{max} = 1/(1 + e^{(V_{1/2} - V)/s}), \quad (3)$$

where $V_{1/2}$ is the potential of half maximal activation, and s is the slope, all in mV. Unless otherwise specified, data are reported as averages from at least four independent measurements, and

error bars are SEMs. Fitting parameters are shown with standard error (SE). Each average comes from measurements performed on at least two distinct batches of cells.

Concentration dependences were fitted with the Hill equation (Eq. 4):

$$\%_{inhib} = \%_{max}[L]^h \big/ \left([L]^h + IC_{50}^h\right), \tag{4}$$

where $\%_{inhib}$ is the percentage of inhibition at the ligand concentration $[L]$, $\%_{max}$ is the percentage of maximal inhibition (assumed to be 100%), IC_{50} is the half maximal inhibitory concentration, and h is the Hill coefficient.

State model of HIF block

The process of HIF-mediated Hv1 inhibition was simulated with Berkeley Madonna 9.1 (Marcoline et al., 2020) using the four-state model shown in Fig. 2 A (model S), or the five-state model shown in Fig. S8 (model E). C and O are the fractions of unbound channels in the closed and open states, respectively. Both models assume that the inhibitor interacts differently with the channel in the closed and open states. B and T (model S) or B_1, I_2, and T_2 (model E) are the fractions of channels interacting with the inhibitor in the modalities described in the Results. The total number of channels ($N = N_C + N_O + N_B + N_T$ for model S or $N = N_C + N_O + N_{B1} + N_{I2} + N_{T2}$ for model E) was set to remain constant during the simulation ($dN/dt = 0$). Assuming that the rate constants under the simulated conditions remain the same at equilibrium, detailed balance principle was applied to satisfy the following relationships: $(k_{CO} \cdot k_{OB} \cdot k_{BT} \cdot k_{TC}) / (k_{OC} \cdot k_{BO} \cdot k_{TB} \cdot k_{CT}) = 1$ for model S or $(k_{CO} \cdot k_{OI2} \cdot k_{I2T2} \cdot k_{T2C}) / (k_{OC} \cdot k_{I2O} \cdot k_{T2I2} \cdot k_{CT2}) = 1$ and $(k_{OB1} \cdot k_{B1I2} \cdot k_{I2O}) / (k_{B1O} \cdot k_{I2B1} \cdot k_{OI2}) = 1$ for model E. A common feature of the two models is that the T ↔ B and T_2 ↔ I_2 transitions are significantly slower than the C ↔ O transition. For simplicity, the deceleration was applied uniformly at all voltages by multiplying the voltage-dependent rate constants k_{CO} and k_{OC} by nonvoltage-dependent parameters (fs) so that $k_{TB} = f_{TB} \cdot k_{CO}$, $k_{BT} = f_{BT} \cdot k_{OC}$, $k_{T2I2} = f_{T2I2} \cdot k_{CO}$, and $k_{B2T2} = f_{B2T2} \cdot k_{OC}$. The integration method was Runge-Kutta 4 with step size of either 0.01 or 0.02 s. The models calculated the proton current as a function of applied membrane potential (V_m in mV) through the equation $I = G_{max} \cdot O \cdot V_m$, where $O = N_O/N$, and G_{max} is the maximal conductance in pA/mV (the reversal potential was assumed to be 0 mV to match experimental conditions). Simulation parameters for HIF-mediated inhibition of Hv1 WT are reported in Fig. S2 for model S and Fig. S8 for model E. Simulation parameters for HIF-mediated inhibition of Hv1 F150A with model S are reported in Fig. S7. The shift in the Hv1 voltage dependence of activation caused by HIF (Fig. S5 A) means that the simulation conditions described here should be used only when strong membrane depolarizations ($V_m > 100$ mV) are applied to monitor channel inhibition. If lower membrane potentials are used, the additional reduction in current produced by the G-V shift needs to be considered (see Discussion).

Docking calculations and MD simulations

HIF was docked into a previously described closed-state model of the human Hv1 VSD (Geragotelis et al., 2020) using AutoDock Vina (Trott and Olson, 2010). Docking was performed using 100 protein configurations extracted from the last part (∼3 µs) of an 8-µs simulation at 0 mV (Geragotelis et al., 2020). The membrane and all water molecules were removed during docking. The search space included the entire intracellular vestibule up to D112 (total volume search space: 33 Å × 33 Å × 24 Å). The starting pose for MD simulations was chosen from visual evaluation of the ligand's proximity to putative binding site residues based on experimental data (proximity of the five-membered ring to D174 and proximity of the fluorinated ring to W207). HIF was parameterized as described in Zhao et al. (2021). MD simulations of HIF-bound Hv1 VSD embedded in a solvated lipid bilayer made of 1-palmitoyl-2-oleoylphosphatidylcholine (POPC) were performed using NAMD 2.13 (Phillips et al., 2005). The CHARMM36 force field (Klauda et al., 2010; MacKerell et al., 1998) was used for both protein and lipid, and the TIP3P model was used for water (Jorgensen et al., 1983). The system was first energy minimized using the conjugate gradient algorithm then equilibrated for 8 ns in the canonical (constant moles, volume, temperature [NVT]) ensemble at a temperature of 300 K maintained by the Langevin thermostat with a damping constant of 1 ps^{-1}. All simulations were run with a 2-femtosecond (fs) time step, with constrained bonds to hydrogen atoms using the SHAKE algorithm, and with periodic boundary conditions applied in all directions. Bonded interactions and short-range forces were calculated every 2 fs, and long-range forces were calculated every 4 fs. Long-range electrostatic interactions were treated using the particle mesh Ewald algorithm (Essmann et al., 1995), while short-range Lennard-Jones and coulombic interactions were calculated with a cutoff of 12 Å and a switching function applied beyond 10 Å. The system was simulated under 0 mV membrane potential. Following NVT equilibration, dynamics were run for 120 ns in the isothermal-isobaric ensemble at a pressure of 1 atm while applying the Langevin piston method (Feller et al., 1995; Martyna et al., 1994) with an oscillation period of 200 fs and a damping time of 100 fs. All other simulation settings were maintained as described for the NVT stage.

Online supplemental material

Fig. S1 compares the recovery from HIF-mediated inhibition at two depolarization frequencies. Fig. S2 provides the kinetic parameters used to simulate HIF-mediated inhibition of Hv1 WT with model S. Fig. S3 compares simulations based on model S to corresponding experimental data. Fig. S4 shows the effect of voltage on the apparent binding of HIF to the C state. Fig. S5 shows the effect of HIF on the G-V relationship of Hv1 WT. Fig. S6 shows the effects of B or T destabilization on the time course of HIF-mediated inhibition predicted by model S. Fig. S7 shows simulations of the time course of HIF-mediated inhibition of Hv1 F150A. Fig. S8 compares simulations performed with model E and with model S. Fig. S9 shows a sequence alignment of segments S2 and S3 from representative human VSD-containing proteins.

Results

HIF-mediated inhibition of Hv1 has two kinetically distinct components

In Hv1 WT, the processes of 2GBI binding and unbinding are faster than the process of channel opening (time scale of seconds;

Hong et al., 2013). Accordingly, Hv1 proton currents measured from inside-out patches were rapidly reduced to a stable inhibited level (close to 50% of the original current) upon perfusion of 50 μM 2GBI in the intracellular compartment, and they returned to their original level in a few seconds upon 2GBI washout (Fig. 1 A). When tested at the same concentration, ABI inhibited the proton current to a smaller extent but with similar kinetics (Fig. 1 A). In contrast, the time course of Hv1 inhibition by 50 μM HIF displayed an initial fast decrease in proton current followed by a further decrease on a much longer time scale (Fig. 1 B). The kinetics of inhibition could be best fitted by a double-exponential decay (Eq. 1) with time constants $\tau_{fast} < 5$ s and $\tau_{slow} > 40$ s (Fig. 1 C). After removal of the inhibitor, the current recovered only slowly (Fig. 1 B). The time course of recovery was fitted with a single-exponential function (Eq. 2), which produced a time constant $\tau_{off} \geq 80$ s (Fig. 1 C). To check whether the time course of inhibition depended on the relative time spent in the open state during HIF application, we performed measurements in which the RDT (see Materials and methods) was varied from 0.1 (one tenth of the time in the O state) to 0.5 (half the time in the open state). Membrane patches were not as long lasting at high depolarization frequencies as they were at low depolarization frequencies. As a result, it was not possible to follow the time course of inhibition for high RDTs as long as for low RDTs. Nevertheless, the data could be well fitted by a double-exponential function in all cases, providing fast and slow time constants.

We found that the time course of inhibition, and τ_{slow} in particular, did not show a clear dependence on RDT (Fig. 1, B and C). However, the recovery from inhibition upon washout became faster (τ_{off} decreased) as RDT increased (Fig. 1 C). To confirm that the recovery from inhibition is a function of the relative depolarization time during washout (RDT$_{off}$), we used a protocol with RDT$_{on} = 0.2$ to monitor the current decay induced by 100 μM HIF. Once the inhibition reached ~90%, we removed the inhibitor while simultaneously switching to a different recording protocol with RDT$_{off}$ values of either 0.1 or 0.5 (Fig. S1, blue and pink traces, respectively). We fitted each recovery of inhibition with a single-exponential function and confirmed that the time constant τ_{off} decreased as RDT$_{off}$ increased (Fig. S1, bar graph), suggesting that more frequent channel openings allow for faster HIF unbinding.

We then measured the time courses of channel inhibition by 50 μM of HIF analogues HIF$_{NF}$, HIF$_{NH}$, HIF$_{OH}$, and HIF$_{EN}$, which differ from HIF in the way the phenyl ring is substituted or connected to the common 2-aminoimidazole moiety (Zhao et al., 2021). The inhibition kinetics for HIF$_{NF}$, HIF$_{NH}$, and HIF$_{EN}$ resembled the one for HIF, with fast and slow components (Fig. 1, D, E, and G), and could be fitted with a double-exponential decay (Fig. 1 H). On the other hand, the inhibition kinetics for HIF$_{OH}$ did not have a significant slow component (Fig. 1 F) and could be fitted by a single-exponential decay with a time constant similar to τ_{fast} for HIF (Fig. 1 H). These findings indicate that (1) HIF compounds interact with Hv1 via two processes that are kinetically distinct and (2) the hydroxyl group in HIF$_{OH}$ strongly reduces the slow inhibitory process that distinguishes HIF compounds from 2GBI and ABI.

Mechanism of Hv1 inhibition by HIF: A kinetic model
The simplest kinetic scheme that can describe Hv1 inhibition by 2GBI and ABI involves three states: closed (C), open (O), and blocked (B) with S4 down in the C state and up in the O and B states (Fig. 2, A and B). The kinetic properties of the inhibition process and the position of the binding site within the VSD are consistent with a mechanism in which the channel can bind the inhibitor only in the O state and cannot close until the binding site is vacated (Chamberlin et al., 2014; Geragotelis et al., 2020; Gianti et al., 2016; Hong et al., 2013). Hv1 inhibition by HIF and its analogues occurs in at least two steps with distinct kinetic components. As a result, a model with more than three states is required for its description. We found that the addition of a fourth state connected to the B and C states and with S4 down (Fig. 2, A and B) was sufficient to explain the main properties of the HIF-mediated inhibition (see Materials and methods and Figs. S2 and S3 for details). We refer to the additional state as "trapped" (T) because the kinetic rates associated with the B ↔ T and C ↔ T transitions are much slower than channel activation at the tested voltage and the process of open-channel block (C ↔ O and O ↔ B transitions; Fig. S2 and Fig. 2 B). The four-transition scheme shown in Fig. 2 A (hereafter referred to as model S) successfully reproduced the experimental time course of channel inhibition with its two components and the slow recovery after HIF removal (Fig. 2 C). Changing RDT$_{on}$ from 0.5 to 0.1 produced only minor changes in τ_{slow} in the simulated inhibition, in agreement with the experimental observation (Fig. S3, A and B). Furthermore, the model replicated the dependence of the recovery from inhibition on RDT$_{off}$ (Fig. S3 C) and the overall concentration dependence of inhibition (Fig. S3 D).

The proposed mechanism of HIF inhibition implies that the compound can bind the VSD in the C state. To confirm this point, we assessed channel inhibition under pulsed application of the inhibitor (100 μM for 3 s; Fig. 2 D). The membrane was kept at −40 mV during each application, and the effect on the proton current was measured after each pulse with a depolarization step at +120 mV (Fig. 2 E). Control pulses of 100 μM 2GBI were applied first to verify that the inhibitor could be completely removed from the intracellular solution between consecutive depolarizations (Fig. 2, E and F). The time course of inhibition under pulsed conditions is shown in Fig. 2 F (teal squares). The current slowly decayed following a single-exponential function with $\tau = 46 \pm 4$ s, which is in good qualitative agreement with the kinetics of inhibition predicted by model S (black circles). The current decay predicted by a four-state model similar to model S but lacking the C ↔ T transition is also shown (Fig. 2 F, pink circles).

We then tested whether the resting membrane potential used to keep the channel closed affected the inhibition under pulsed conditions. We performed measurements at −80 mV (Fig. S4, blue circles), a voltage at which the C state is much more stable than the O state, and at 0 mV (Fig. S4, green circles), a voltage near the opening threshold (foot of the G-V curve). We found that HIF inhibited the channel to a greater extent at 0 mV (more efficient trapping) compared with −80 mV (55 ± 3% at 0 mV, 33 ± 4% at −80 mV). Hv1 is known to transition through multiple C states before opening (Carmona et al., 2018; DeCoursey and Cherny, 1994; Gonzalez et al., 2010; Tombola et al., 2010; Villalba-Galea, 2014). The dependency of channel inhibition on resting membrane potential might reflect different populations of closed channels with different affinities for HIF. Additionally,
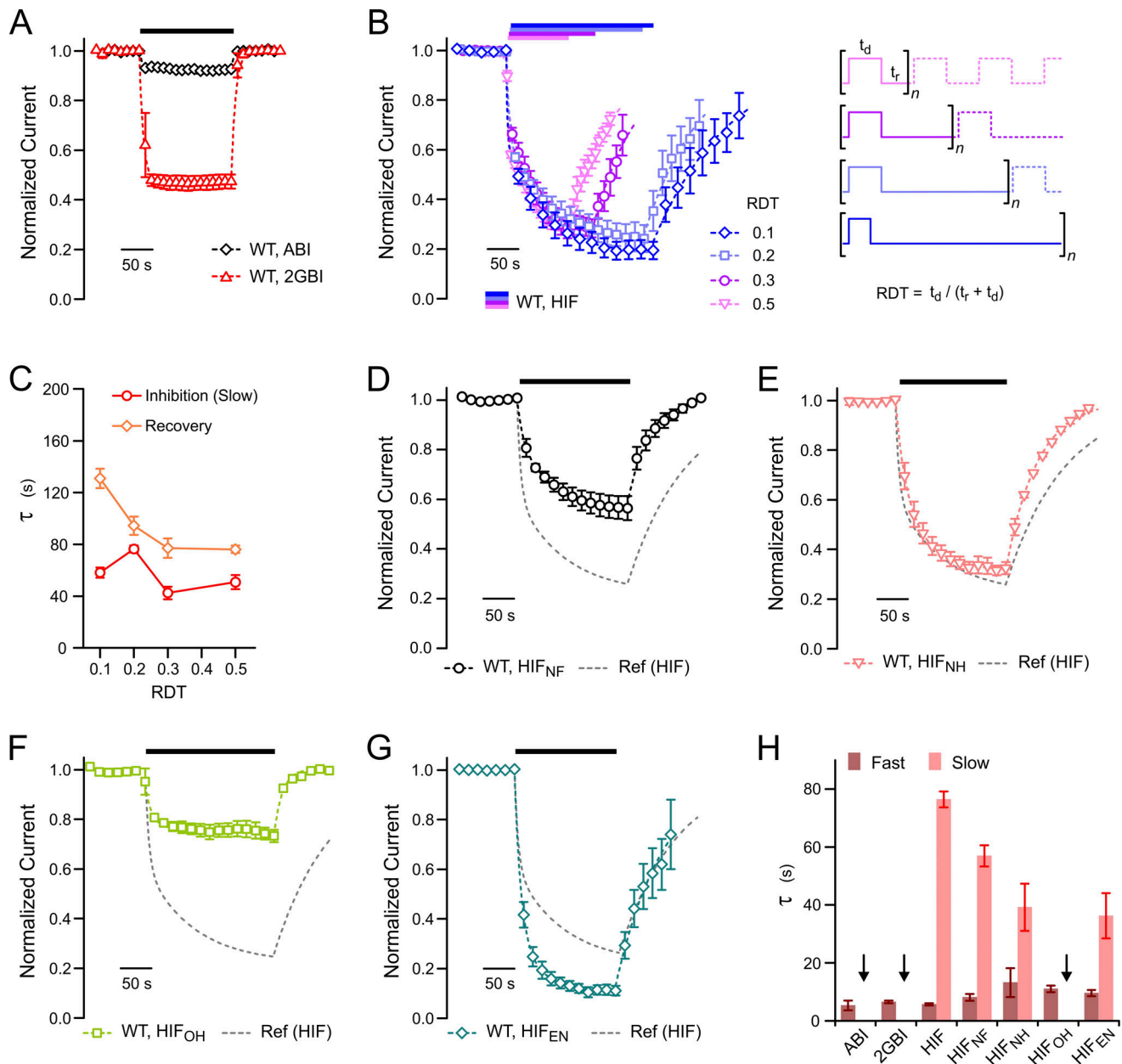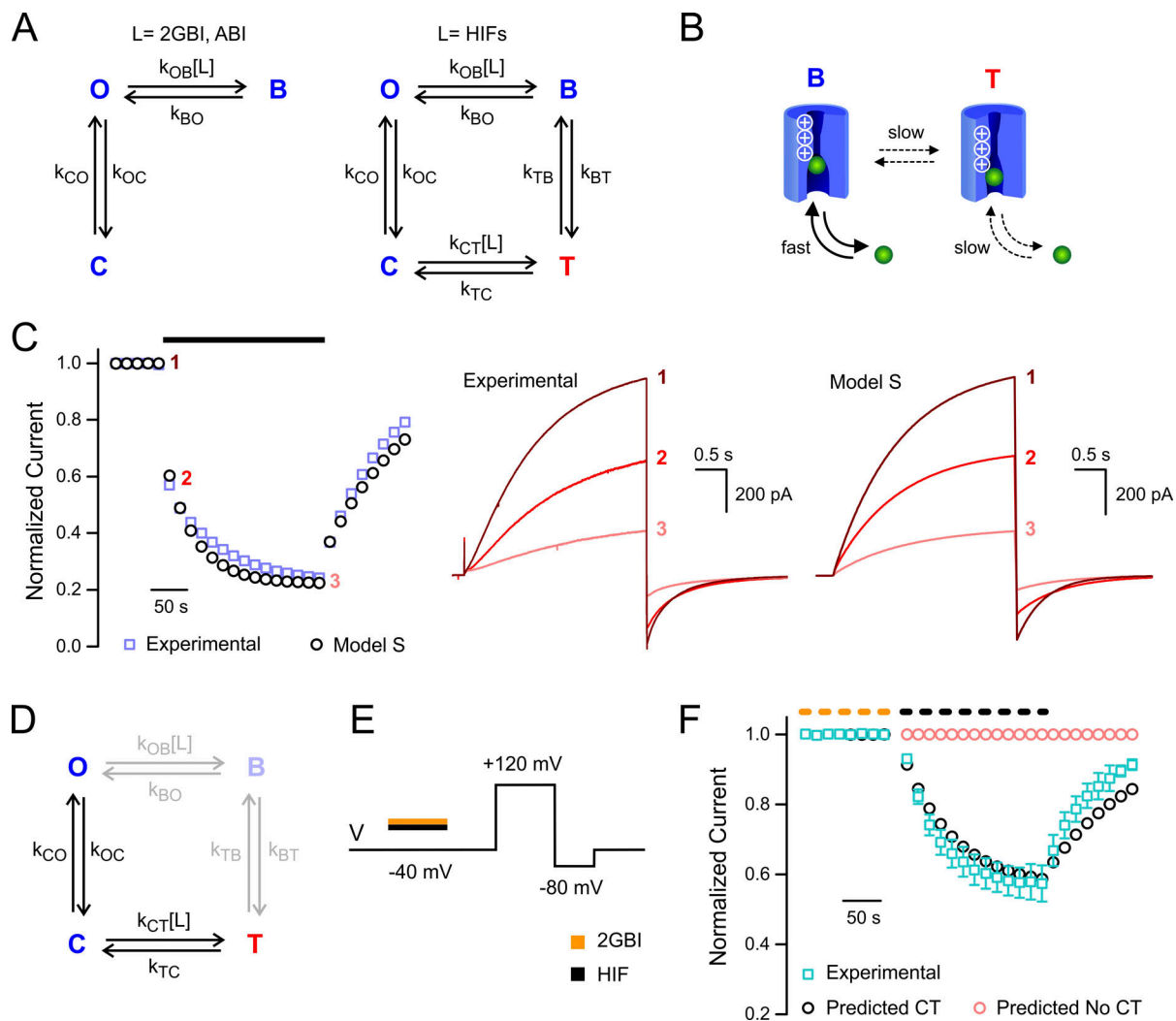
Figure 1. **Kinetics of Hv1 inhibition by HIF compounds compared with ABI and 2GBI. (A)** Time courses of channel inhibition by 50 μM ABI or 2GBI. The black bar indicates the presence of the inhibitor in the bath solution. Currents were measured in inside-out patches from oocytes expressing Hv1 WT. The membrane was depolarized to +120 mV from a holding potential of −40 mV, pH_i = pH_o = 6.0. Data points are averages from three independent measurements for each inhibitor ± SEM. **(B)** Time courses of channel inhibition by 50 μM HIF under different RDT conditions. Horizontal bars indicate the presence of the inhibitor in the bath solution. Currents were measured as in A following voltage protocols with variable RDT. Data points are averages from n independent measurements for each RDT condition ± SEM (n = 7, 7, 5, 8 for RDT = 0.1, 0.2, 0.3, 0.5, respectively). Fitting curves are shown as dashed lines (see Materials and methods). **(C)** Time constants of HIF-mediated inhibition of Hv1 WT (slow component, red) and recovery (orange) as a function of RDT from fits of data points in B. Error bars are SE. **(D–G)** Time courses of inhibition of Hv1 WT by the indicated compounds compared with HIF (gray dashed line). All compounds were tested using a voltage protocol with RDT = 0.2. Black bars indicate the presence of 50 μM inhibitor in the bath solution. Data points are averages from n independent measurements for each inhibitor (n = 5, 4, 4, 5 for HIF_{NF}, HIF_{NH}, HIF_{OH}, HIF_{EN}, respectively). Error bars are SEM. **(H)** Time constants τ_{fast} and τ_{slow} from fitting of time courses of inhibition reported in A and B and D–G. Error bars are SE. Black arrows indicate lack of the slow component of channel inhibition. Ref, reference.

the processes of HIF binding and unbinding could be intrinsically voltage dependent.

Another implication of the proposed mechanism of HIF inhibition is that the closed VSD could be stabilized by the bound inhibitor, making the channel more difficult to open.

We verified whether this stabilization affected the channel voltage dependence of activation by comparing the G-V curve measured in the presence of 50 μM HIF to the G-V curve measured in the absence of inhibitor (Fig. S5 A). We did observe an ~15-mV shift to more positive potentials in the $V_{1/2}$ of

Figure 2. Four-state model replicates Hv1 inhibition by HIF. (A) Kinetic schemes for modeling Hv1 inhibition by the indicated compounds. For ABI and 2GBI, the scheme involves three states: O, B, and C. For HIFs, an additional state, T, is required (model S). **(B)** Correspondence between B and T states with open and closed VSD configurations. The inhibitor can quickly bind and unbind from the open VSD (S4 in the activated position). The inhibitor can slowly bind and unbind from the closed VSD (S4 not activated). White positive charges represent S4 arginines. **(C)** Simulated time course of HIF-mediated Hv1 inhibition and recovery using model S compared with experimental data from Fig. 1 B. For modeling parameters, see Fig. S2 A. Black bar indicates the presence of 50 µM HIF in the bath compartment. Current traces generated by the model at time points 1, 2, and 3 are compared with the current traces measured experimentally at the corresponding time points. **(D)** Kinetic scheme in effect when the channel is exposed to HIF in the C state only (minimized fraction of channels in the B state). **(E)** Protocol used to expose the channel to HIF selectively in the C state. Yellow and black bars indicate the presence of 100 µM 2GBI and HIF, respectively, in the bath compartment (each sweep was 15 s long with the depolarization step lasting 3 s; see also Fig. S2 B). **(F)** Time course of channel inhibition and recovery under protocol E as delineated by teal squares. Yellow and black dashed lines indicate recurring transient exposure to 2GBI or HIF, respectively. Data points are averages from seven independent measurements ± SEM. Black and red circles indicate normalized current predicted by the four-state model in the presence and absence of the C ↔ T transition, respectively. For modeling parameters, see Fig. S2 B.

activation, consistent with a stabilization of the closed VSD induced by HIF. This finding contrasts with the lack of G-V shift observed with 2GBI under equivalent conditions (Fig. S5 B), which is expected, as 2GBI is an open channel blocker unable to stabilize the C state (Hong et al., 2013). It should be noted that our kinetic modeling does not account for an HIF-induced G-V shift (see Discussion).

Structural determinants of Hv1 inhibition by HIF

The requirement for two distinct inhibitor-bound states (B and T) in the kinetic model of HIF inhibition could be easily

explained by assuming that HIF binds the VSD in two different modalities or binding sites, which we refer to as sites 1 and 2. Under this assumption, HIF interaction with site 1 would be responsible for the fast component of the time course of inhibition (transition to state B), the interaction with site 2 would be responsible for the slow component (transition to state T), and the inability of 2GBI to interact with site 2 would provide a simple justification for the lack of a slow component in its time course of inhibition. Accordingly, model S predicts that a destabilization of state T (interaction with site 2) will eliminate or strongly reduce the slow component of channel inhibition

(Fig. S6 A), whereas the destabilization of state B (interaction with site 1) will eliminate or strongly reduce the fast component of channel inhibition (Fig. S6 B).

To test these possibilities and gain insight into the nature of the two sites within the channel protein, we compared the time course of inhibition of various Hv1 mutants to Hv1 WT (HIF = 50 µM) and assessed the effect of each mutation on the fast and slow components of the current decay. First, we measured the effect of HIF on the proton current of a monomeric version of Hv1, a chimeric channel in which the N- and C-termini are replaced with the corresponding parts of the voltage-sensitive phosphatase CiVSP (Fig. 3 A; Hong et al., 2015; Tombola et al., 2008). We found that the kinetics of inhibition was perturbed compared with WT. The time constants for the two components (τ_{fast} and τ_{slow}) were too close to each other to be reliably resolved by a double-exponential fit. As a result, the time course of inhibition was fitted with a single-exponential function. Despite the differences in kinetics, the extent of inhibition in the chimeric channel was not reduced (Fig. 3 A), indicating that a functional intersubunit interface is not required for HIF binding.

Hv1 residues at positions 112, 150, 181, and 211 were previously shown to participate in 2GBI binding when the channel is in the open conformation (Hong et al., 2014). We assumed that some of these residues could interact with HIF as well. We measured the time courses of HIF-mediated inhibition of mutants D112E, F150A, S181A, and R211A and compared them to the time course of inhibition of WT (Fig. 3, B–F). We found that the fast component of the inhibition process was eliminated by mutation D112E, while the slow component was unaffected (Fig. 3 B). The fast component was strongly enhanced by mutation F150A to the point that the concentration of HIF had to be reduced from 50 µM to 100 nM to maintain an inhibition level comparable to WT (Fig. 3 C). The effects of mutations D112E and F150A closely resembled those previously observed with 2GBI-mediated inhibition (Hong et al., 2014; Hong et al., 2013), indicating that both HIF and 2GBI interact with a site comprising D112 and F150.

The R211A mutation accelerated the slow component of HIF-mediated inhibition (64% reduction in τ_{slow}) and decreased steady-state remaining current (15% higher inhibition; Fig. 3, E and F). S181A had an impact similar to R211A but smaller in magnitude (26% reduction in τ_{slow}, 7% higher inhibition; Fig. 3, D and F). The fast component of inhibition was not significantly altered by the two mutations, suggesting that HIF and 2GBI may differ in the way they interact with R211 and S181.

D112 is located in the narrowest part of the Hv1 proton conduction pathway, approximately halfway across the membrane where it serves as selectivity filter (Berger and Isacoff, 2011; Musset et al., 2011; Takeshita et al., 2014). Earlier work showed that the residue is accessible to arginine mimics from the intracellular side of the membrane only when the channel is open (Geragotelis et al., 2020; Hong et al., 2014; Hong et al., 2013). The selective effect of mutation D112E on the fast component of HIF-mediated inhibition resembles what is predicted by model S when the B state is destabilized (Fig. S6 A) and suggests that HIF interaction with D112 occurs in the O state at a location consistent with site 1. The effect of mutation F150A is predicted by

model S when binding to site 1 is strongly stabilized and the gating process is accelerated compared with Hv1 WT (Fig. S7 A). The biphasic shape of the current traces (increase followed by a decrease) in the presence of HIF indicates that the inhibitor must wait for the channel to open in order to interact with site 1 (Fig. S7 B). This behavior was described earlier for 2GBI and its analogues (Hong et al., 2013; Hong et al., 2015).

The finding that HIF interaction with site 1 in the O state involves D112 and F150 raises the question of how the positively charged inhibitor interacts with the C state (site 2). Besides D112, Hv1 contains four other acidic residues in the transmembrane region at positions 153, 171, 174, and 185. We tested for potential roles of these residues in HIF binding by measuring the time course of inhibition of channels mutated at each of the four positions. In the mutant selection process, we first tried conservative charge-neutralizing substitutions E/Q or D/N or alanine substitutions. However, we found that mutations at position 174 other than the charge-preserving D/E substitution resulted in proton currents too small to be reliably measured in inside-out patch configuration. In addition, mutation E153C resulted in better expression than the more conservative substitution E153Q. As a result, we tested HIF inhibition on channels carrying mutations E153C, E171Q, D174E, or D185A (Fig. 4).

The total extent of inhibition did not decrease in the E153C mutant, but the relative contribution of the slow component, measured as $c_{slow} / (c_{fast} + c_{slow})$ from Eq. 1, increased from 0.51 of the WT to 0.80 at the expense of the fast component (Fig. 4 A). Additionally, we observed a significant slowdown in the recovery from inhibition (Fig. 4 A, black arrow; τ_{off} [WT] = 94 ± 7 s; τ_{off} [E153C] = 294 ± 57 s). These findings point to a reduced ability of Hv1 E153C to release HIF from its binding site and suggest a relative stabilization of the T state over the B state caused by the mutation.

In the E171Q and D174E channels, the extent of HIF inhibition was reduced (46% and 35% reduction, respectively; Fig. 4, E and F), and τ_{slow} increased to such an extent (>200 s) that an accurate value could no longer be determined by double-exponential fit. Furthermore, mutation D174E caused a marked acceleration of the recovery from inhibition (τ_{off} [WT] = 94 ± 7 s; τ_{off} [D174E] = 37 ± 6 s; Fig. 4 F, black arrow). Mutation D185A, on the other hand, did not appreciably affect the extent or time course of HIF-mediated inhibition (Fig. 4 G). The effect of mutation D174E and, to a smaller extent, the effect of D171Q resemble what is predicted by model S when the T state is destabilized (Fig. S6 B), consistent with the involvement of D174 and E171 in the process of HIF trapping in the closed VSD (interaction with site 2).

D174 is part of a network of charged residues forming electrostatic interactions in the intracellular vestibule of the channel (Chamberlin et al., 2014; Ramsey et al., 2010; Randolph et al., 2016; Takeshita et al., 2014), and it is located in the proximity of E171 and K157. The perturbation of HIF-mediated inhibition by neutralization of E171 suggested that a similar perturbation could be induced by neutralization of K157. We measured proton currents from Hv1 K157Q in the presence of 50 µM HIF and found that the time course of inhibition resembled the one from the E171Q mutant, with a very low transition rate to the T state (τ_{slow} > 200 s) and reduced extent of inhibition (46% reduction;
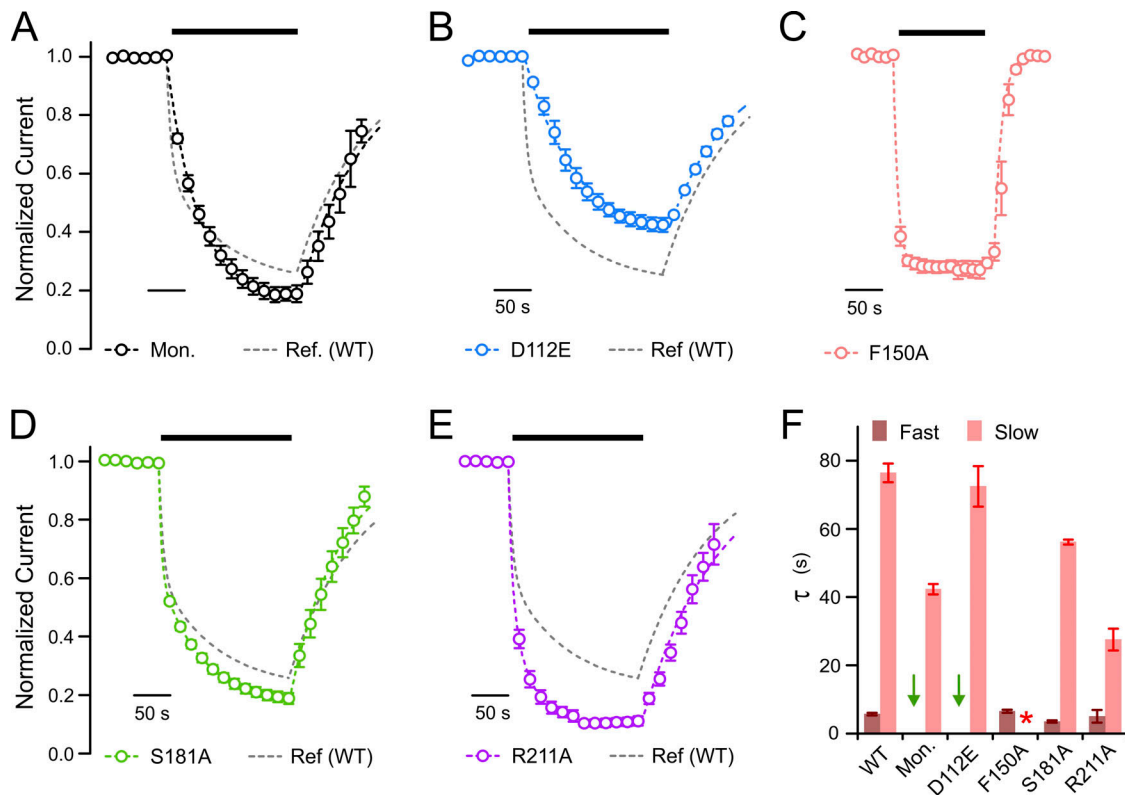
Figure 3. Structural determinants of HIF-mediated inhibition: open VSD. (A) Time course of inhibition of monomeric (Mon.) Hv1 by 50 µM HIF compared with WT (dimeric) channel. The fast component is slowed down and cannot be resolved from the slow component. **(B)** Time courses of inhibition of Hv1 D112E by 50 µM HIF show lack of fast component. **(C)** Time courses of inhibition of Hv1 F150A by 100 nM HIF display enhanced fast component. **(D)** Time courses of inhibition of Hv1 S181A by 50 µM HIF show only minor deviations from WT. **(E)** Time courses of inhibition of Hv1 R211A by 50 µM HIF display accelerated slow component and increased steady-state inhibition. Data points in A–E are averages from n independent measurements ± SEM (n = 7, 4, 5, 5, 9 for Mon., D112E, F150A, S181A, R211A, respectively). Black bars indicate the presence of the inhibitor in the bath compartment. Fitting curves are shown as dashed lines with colors matching the corresponding symbols. Gray dashed lines represent current decay and recovery of Hv1 WT. **(F)** Time constants τ_{fast} and τ_{slow} from fitting of time courses of channel inhibition reported in A–E. Error bars are SE. Green arrows indicate either nonresolved (Mon.) or missing (D112E) fast component. Red asterisk indicates lack of slow component. Ref, reference.

Fig. 4 C). In contrast, mutation of residue F156, next to K157, did not result in any significant change in HIF inhibition (F156A; Fig. 4 B). Based on these findings, we propose that the neutralization of E171 or K157 affects the electrostatic network that includes D174 and destabilizes the VSD–HIF interactions in the T state.

Separating protein movements from ligand rearrangement

In model S, S4 moves from the "down" conformation of the T state to the "up" conformation of the B state upon membrane depolarization, while the inhibitor concurrently moves from site 2 to site 1. So, the T ↔ B transition is a combination of two processes, one involving the protein and one involving the ligand. To emphasize the latter, the T and B states can be renamed as T_2 and B_1, respectively (Fig. S8 A). Merging the two processes in one transition simplifies the description of HIF-mediated inhibition, but it is not a necessary condition. In the alternative model shown in Fig. S8 A (model E), for example, the movement of S4 is separated from the movement of the ligand. Upon depolarization, T_2 leads to an intermediate state I_2 in which S4 is in the up conformation but the ligand is still interacting with site 2 (Fig. S8 B). The ligand can then move to site

1 from I_2 to form B_1. This model also implies the presence of a transition O ↔ I_2 in which the ligand binds site 2 in the VSD open conformation. We found that model E can replicate the predictions of model S when the T_2 ↔ I_2 transition (protein conformational change) is much slower than the I_2 ↔ B_1 transition (rearrangement of the ligand). For the purpose of this work, model E did not offer significant advantages over model S. However, model E can be further implemented to explain aspects of Hv1 inhibition by HIFs, and potentially other compounds that bind site 2, which have not been investigated here (see Discussion).

HIF interactions with site 2

To better understand the interactions between HIF with the closed VSD at site 2, we used a computational approach based on the structural model of the Hv1 VSD in the closed conformation generated from the 3WKV crystal structure (Geragotelis et al., 2020; Takeshita et al., 2014) and equilibrated in a solvated POPC lipid membrane at 0 mV (see Materials and methods). We first used the program AutoDock Vina (Trott and Olson, 2010) to search for potential binding sites within the VSD intracellular vestibule. We set the search space to include the entire vestibule
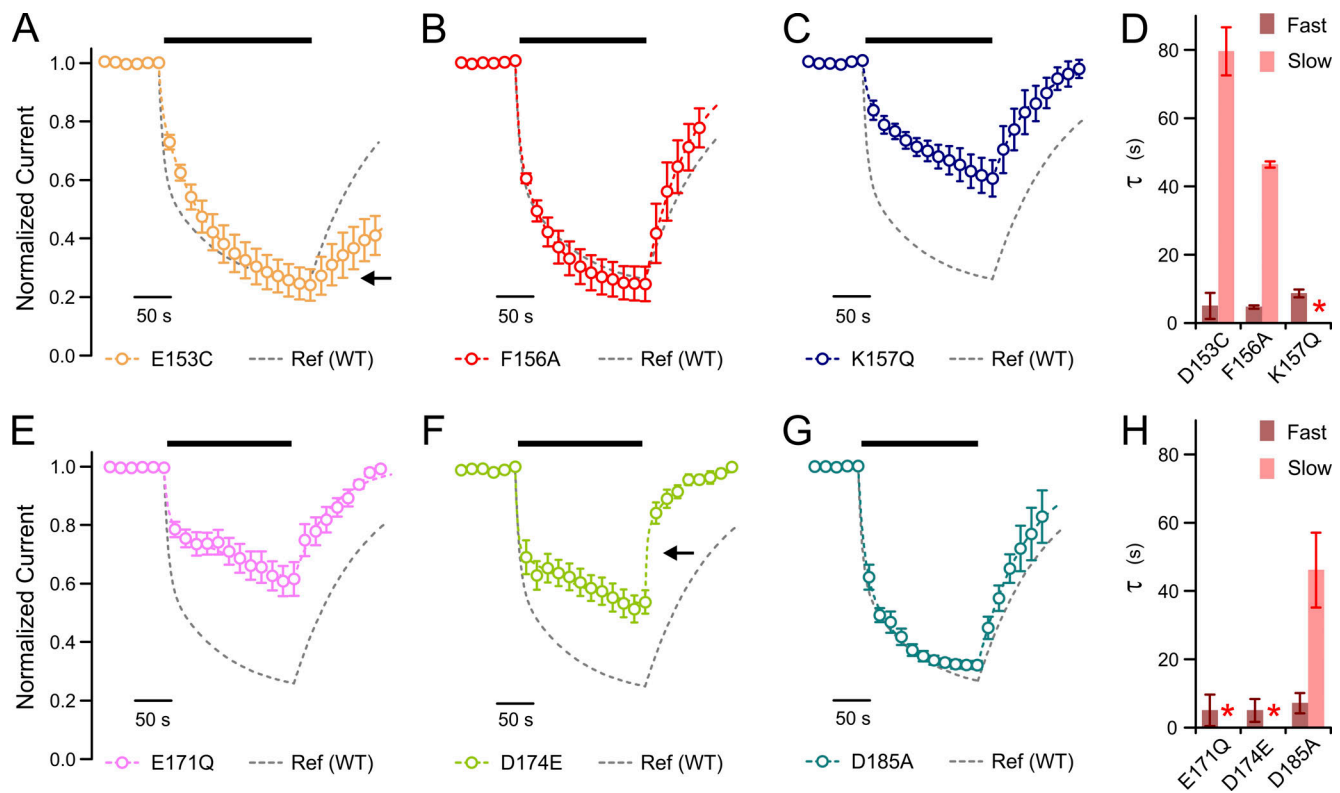
Figure 4. **Structural determinants of HIF-mediated inhibition: closed VSD. (A–C)** Time courses of inhibition of Hv1 E153C, F156A, and K157Q by 50 μM HIF. Black bars indicate the presence of the inhibitor in the bath compartment. Data points are averages from n independent measurements ± SEM (n = 6, 7, 5 for E153C, F156A, K157Q, respectively). K157Q reduces the extent of inhibition and decelerates current decay. E153C affects primarily the rate of recovery from inhibition (black arrow in A). F156A has negligible effects. **(D)** Time constants τ_{fast} and τ_{slow} from fitting of time courses of channel inhibition reported in A–C. Error bars are SE. **(E–G)** Time courses of inhibition of Hv1 E171Q, D174E, and D185A by 50 μM HIF. Black bars indicate the presence of the inhibitor in the bath compartment. Data points are averages from n independent measurements ± SEM (n = 7, 8, 6 for E171Q, D174E, D185A, respectively). E171Q and D174E perturb the time course of channel inhibition significantly. In addition, D174E strongly accelerates recovery from inhibition (black arrow in F). D185A has negligible effects. **(H)** Time constants τ_{fast} and τ_{slow} from fitting of time courses of channel inhibition reported in E–G. Error bars are SE. Red asterisks in D and H indicate τ_{slow} > 200 s (too slow to be accurately quantified). Ref, reference.

and assigned to HIF a positive charge by protonating its five-membered ring. In seven of the nine most stable binding poses, the HIF fluorinated phenyl ring was inserted in the narrowest part of the vestibule and pointed toward S4 residues W207 and R208, whereas the protonated 2-aminoimidazole ring was located in the wider part of the vestibule and interacted with the electrostatic network in the proximity of D174. An example of such poses is shown in Fig. 5 A. We verified whether perturbation at positions 207 and 208 affected HIF-mediated inhibition by testing conservative mutations W207Y and R208K and found that Hv1 W207Y was inhibited to a smaller extent compared with Hv1 WT (38% reduction; Fig. 5 B), mostly due to a strong decrease in the transition rate to the T state (τ_{slow} > 200 s; Fig. 5 D). R208K, on the other hand, had more subtle effects; the extent of inhibition was slightly increased compared with WT, but the fast kinetic component could no longer be resolved from the slow component (Fig. 5, C and D). We were unable to measure proton currents from Hv1 channels bearing less-conservative mutations at position R208. Overall, these results agree with the docking poses placing the HIF fluorinated ring in the proximity of W207.

We then let the HIF molecule explore the Hv1 intracellular vestibule using unrestrained all-atom MD simulations and the

same structural model of the closed VSD (Fig. 6; Geragotelis et al., 2020). We used the data from molecular docking calculations and the data from mutagenesis experiments to set up the initial pose of HIF within the vestibule (see Materials and methods). The movement of the inhibitor within the putative binding site was then followed for 120 ns. As shown in Fig. 6 A, the ligand center of mass (CM) did not move extensively in the z direction orthogonal to the membrane plane.

Overall, the HIF fluorinated ring dwelt in the deepest part of the vestibule, while the 2-aminoimidazole ring (R5) engaged in hydrogen bonding with the network of charged residues in proximity of D174. The distance between R5 and D174 showed some fluctuations during the simulation (Fig. 6 B). The transient changes in distance (~2 Å) suggest that multiple interactions with the electrostatic network of the vestibule contribute to the stability of HIF binding. Figure 6 C shows the ligand surrounded by a cloud representing the poses assumed during the last part of the trajectory of Fig. 6 A. The results of the simulation confirm that the proposed location of binding site 2 is compatible with the structural model of the closed VSD based on the 3WKV crystal structure. In 3WKV, the Hv1 region comprising the inner ends of S2 and S3 is replaced with the corresponding part of
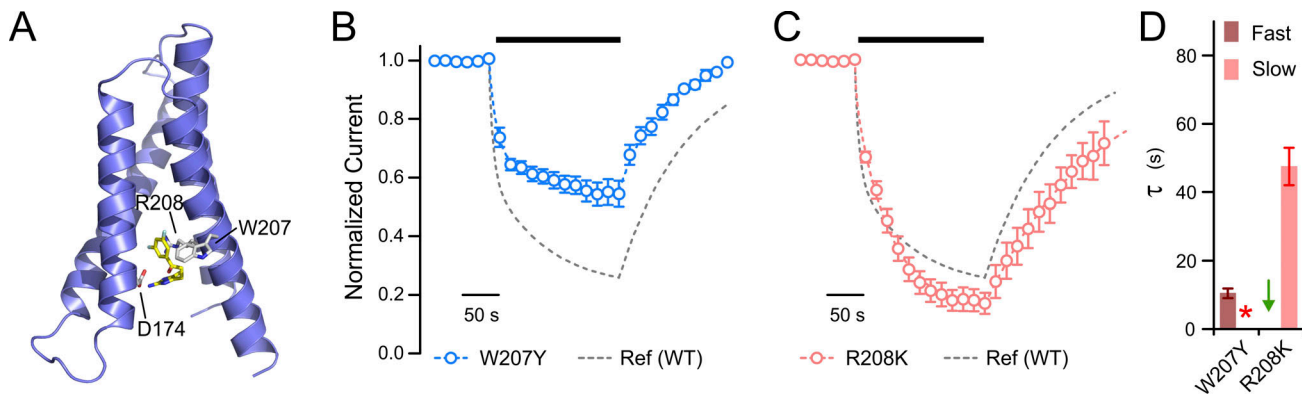
Figure 5. **HIF orientation within the closed Hv1 VSD. (A)** Example of one of the highest scored binding poses predicted by AutoDock Vina for HIF showing the proximity of the ligand fluorinated phenyl ring to W207 and R208 and the proximity of the ligand 2-aminoimidazole ring to D174. **(B)** Time courses of HIF-mediated inhibition for Hv1 W207Y. Black bar indicates the presence of 50 μM HIF in the bath compartment. A reduced slow component in the current decay results in a decreased extent of inhibition compared with WT. **(C)** Time courses of HIF-mediated inhibition for Hv1 R208K. Black bar indicates the presence of 50 μM HIF in the bath compartment. The extent of the perturbation is significantly smaller than for W207Y. Data points in B and C represent averages from n independent measurements ± SEM (n = 7 for W207Y, n = 8 for R208K). **(D)** Time constants τ_{fast} and τ_{slow} from fitting of time courses of channel inhibition reported in B and C. Error bars are SE. Red asterisk indicates τ_{slow} > 200. Green arrow indicates lack of resolvable fast component. Ref, reference.

CiVSP (Takeshita et al., 2014). The difference in sequence between Hv1 and CiVSP in that region is not expected to change substantially the electrostatic network within the VSD since all the charged residues are either identical or with similar charge (E153, K157, E171, and D174 in Hv1 correspond to D164, R168, E183, and D186 in CiVSP, respectively).

Discussion

The complex kinetics of HIF-mediated Hv1 inhibition is well explained by model S and model E with a T state slowly accessible from the closed conformation. We have previously found evidence of an intracellular gate in the Hv1 VSD that regulates 2GBI accessibility to its binding site (Hong et al., 2013). 2GBI binding can only occur when the gate is open, and the gate cannot close until the inhibitor has left the binding site. HIF accessibility to site 1 is assumed to be similarly regulated. Both kinetic models imply that HIF cannot remain bound to site 1 when the gate closes (Fig. 2, A and B; and Fig. S8, A and B). However, the two models differ in the way this is accomplished. In model S, ligand rearrangement and gate closure occur simultaneously. As a result, the ligand leaves site 1 and migrates to site 2 as soon as the gate closes. In model E, the ligand is free to engage either site 1 or site 2 in the open conformation, but the gate can close only when the ligand is in site 2.

HIF binds slowly to the C state in both models to account for the slow component of channel inhibition. Unbinding occurs slowly as well to account for the slow recovery from inhibition. The faster unbinding from the O state (either from B or from B_1 and I_2) provides an explanation for the acceleration of the recovery from inhibition observed at high RDT_{off}. The tight fit of the HIF molecule within the narrow intracellular vestibule (Fig. 6 C) may be the reason for the relatively high energy barriers that the ligand needs to cross to get in and out of site 2 when the gate is closed.

The T ↔ B transition in model S and the $T_2 ↔ I_2$ transition in model E are significantly slower than the corresponding gating

transition in the absence of the inhibitor (C ↔ O), suggesting that the gating process is hindered when the ligand interacts with the VSD. The idea that an arginine mimic bound to the Hv1 VSD can affect S4 movement is in agreement with recent measurements of gating currents from the VSD of Hv1 from *Ciona intestinalis* (Carmona et al., 2018). To enable the measurements, proton conduction was inhibited by placing an arginine at position N264 (corresponding to N214 in human Hv1). The presence of that arginine was proposed to also hinder the movement of S4, causing a discrepancy between the gating charge measured during activation and deactivation (Carmona et al., 2018).

While model S was able to replicate most aspects of the HIF-mediated inhibition examined here, the fact that site 1 and site 2 are rendered mutually exclusive by the opening transition may represent a limitation for simulations involving HIF analogues with particularly steep concentration dependence of inhibition, such as HIF_{EN}. The Hill coefficient for the compound (1.50 ± 0.11; Zhao et al., 2021) is consistent with the presence of more than one cooperative binding site. The finding that the monomeric and dimeric versions of Hv1 display similar Hill coefficients (Zhao et al., 2021) suggests that the sites are on the same subunit. In model E, site 1 and site 2 are not mutually exclusive in the O state. As a result, this model could be further developed to allow the two sites to be occupied simultaneously, thus providing a framework for intrasubunit cooperativity of ligand binding.

When interpreting the steepness of the concentration dependence of inhibition for HIF and its analogues, an experimental caveat needs to be considered. At low concentrations, the binding of these compounds to the C state becomes very slow, which makes it difficult to measure $\%_{inhib}$ at true steady state. The resulting underestimation of $\%_{inhib}$ in the lower concentration range can produce an overestimated Hill coefficient. For example, if Eq. 4 is used to fit the concentration dependence of HIF_{EN}-mediated inhibition (from Zhao et al., 2021) using only
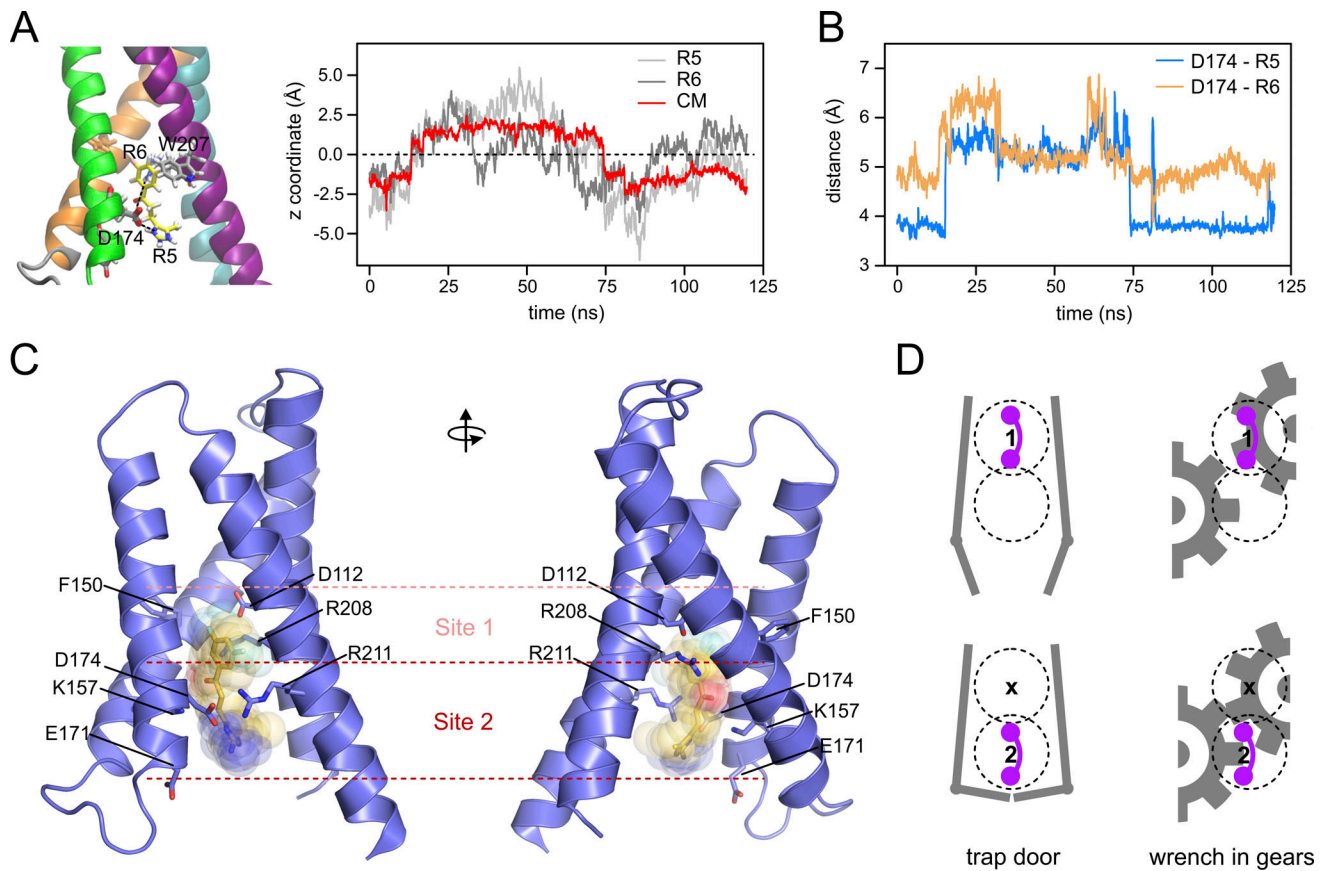
Figure 6. **Proposed HIF binding site in the closed channel and trapping mechanism. (A)** Stability assessment of HIF within the binding site. The change in HIF's CM z coordinate is plotted as a function of time. Dashed line at z = 0 Å represents the average CM z position over the whole trajectory. The CM is evaluated for the entire ligand (red), the five-membered ring alone (R5; light gray), and the six-membered ring alone (R6; dark gray). **(B)** Distance measurements from the γ-carbon atom of D174 to HIF. The D174-to-HIF contacts are measured from D174 to the nearest nitrogen atom of HIF (blue) and to the nearest carbon atom of R6 (orange). **(C)** HIF bound to proposed site 2 in the closed VSD. The site contains an intracellular network of charged residues, including D174, K157, E171, and R211. A representative snapshot is shown of the protein–ligand configuration from the last 40 ns of the MD trajectory. HIF is depicted as sticks, with transparent filled spheres portraying the region that HIF occupies over this portion of the trajectory. The location of site 1 (which includes D112 and F150) is shown here only for reference, as it is not accessible to the ligand in this state. HIF is shown bound to site 1 in the open VSD in Zhao et al. (2021). **(D)** MD simulations of HIF bound to the closed VSD do not support a "trap door" mechanism for trapping (left), as no steric or electrostatic barriers separate the ligand from the exit of the intracellular vestibule. In the simulations, HIF fits inside a pocket formed by side chains of VSD helices within the intracellular vestibule. It is proposed that these side chains act as gear teeth in a wrench in gears trapping mechanism (right).

the three higher concentration points rather than the full set of data points, the estimated Hill coefficient decreases from 1.50 to 1.36. Future studies may investigate whether measuring the steepness of the concentration dependence of inhibition more accurately in the higher concentration range could lead to more reliable estimates of cooperativity.

Model S and model E were used here to simulate the reduction in Hv1 G_{max} induced by HIF. But the ligand also affects the channel G-V curve, shifting it to more positive potentials (Fig. S5 A). Our kinetic models cannot simulate the G-V shift with the current parameters because the T ↔ B and T_2 ↔ I_2 transitions were set to have the same voltage dependence of the C ↔ O transition (see Materials and methods). Future simulations of HIF-mediated inhibition as a function of membrane potential will require k_{TB} or k_{T2I2} to have a voltage dependence distinct from k_{CO} and k_{BT} or k_{I2T2} to have a voltage dependence distinct from k_{OC}. In addition, a mechanism for blocked VSDs to shift the G-V of conducting VSDs will need to be introduced. For example,

one can explore the possibility that in the dimeric channel, HIF bound to one VSD subunit could hinder the opening of an unbound adjacent subunit.

Another aspect of the mechanism of inhibition that warrants further investigation concerns the nature of the I_2 state. If a ligand can stay bound to site 2 in the open VSD, what is the consequence on proton conduction? We assumed here that I_2 is a nonconducting state like B_1. However, site 2 is located in a wider portion of the intracellular vestibule compared with site 1. Therefore, in the open channel, the ligand may not be as efficient at blocking the proton current when bound to site 2 as it is when bound to site 1. This possibility could be further explored if ligands interacting with only site 2 are identified. The existence of a partially conducting I_2 state could also provide an explanation for the HIF-induced G-V shift, if the voltage dependences of the T_2 ↔ I_2 and C ↔ O transitions were different.

The high-energy barriers (~20 kcal/mol at room temperature) that HIF requires to cross in and out of site 2 suggest some

sort of trapping process. The atomistic simulations of HIF docked to the closed Hv1 VSD reveal important molecular details about this process. The simplest way HIF could be trapped in the intracellular vestibule is by a "trap door" mechanism. A cytoplasmic gate could close behind the ligand, thus obstructing the way out of site 2 (Fig. 6 D). However, the entrance of the vestibule in the structural model of the Hv1 VSD is too wide to hinder HIF exit from the vestibule, making the trap door mechanism difficult to justify. On the other hand, during the simulation, HIF remains confined inside a pocket formed by side chains from various VSD helices, which act as teeth of interlocking gears. This finding suggests that the ligand could become trapped via a "wrench in gears" mechanism (Fig. 6 D). If the degree of interlocking were to decrease in the O state, the energy barriers holding HIF in site 2 would be lowered, leaving the ligand free to move to site 1.

In recent years, there has been a renewed interest in the development of peptide ligands and small molecules targeting the VSDs of voltage-gated sodium, potassium, and calcium channels for applications ranging from pain relief to antiarrhythmics (Ahuja et al., 2015; Liin et al., 2016; Liin et al., 2015; Ottosson et al., 2015; Shen et al., 2019; Xu et al., 2019). The binding sites for the majority of these compounds are located on the extracellular portion of the VSD (Ahern et al., 2016; Bosmans et al., 2008; Wulff et al., 2019). However, the recent discovery of a cell-penetrating peptide toxin capable of interacting with the intracellular domain of a TRP channel (Lin King et al., 2019) as well as the development of novel nanobodies (Ingram et al., 2018), open the possibility of targeting the intracellular side of VSDs not only with small molecules but also with larger peptide ligands. Here, we find that HIF interacts with the Hv1 VSD from the intracellular side. The deep region containing site 1 is accessible to ligands like 2GBI and HIF only in the proton-conducting state (up state). It is unlikely that the corresponding region of nonconducting VSDs could be accessible to similar ligands. The packing between helices at the center of those VSDs is expected to be too tight. On the other hand, the shallower site 2 is slowly accessible in nonconducting states (S4 down), raising the prospect that other VSDs could harbor similar intracellular binding sites with slow accessibility. The presence of charged residues that are highly conserved among different channels at site 2 supports this idea (Fig. S9). The tight fitting of site 2 around the HIF molecule shows how the VSD intracellular vestibule can provide specificity of binding to VSD-targeting ligands, a desirable feature for further drug development.

Previous studies found evidence for an allosteric coupling between the Hv1 extracellular binding sites for Zn^{2+} and the peptide toxin AGAP/W38F and the electrostatic network located in the channel intracellular vestibule (De La Rosa et al., 2018; Tang et al., 2020). The proposed mechanism of Hv1 inhibition by these two ligands involves rearrangements of the electrostatic network as a result of ligand binding to the opposite side of the VSD. Here, we show that HIF compounds inhibit Hv1 by a direct interaction with the electrostatic network. Taken together, these findings highlight the importance of the VSD intracellular vestibule as a hotspot for both direct and indirect pharmacological targeting.

References

Ahern, C.A., J. Payandeh, F. Bosmans, and B. Chanda. 2016. The hitchhiker's guide to the voltage-gated sodium channel galaxy. *J. Gen. Physiol.* 147: 1–24. https://doi.org/10.1085/jgp.201511492

Ahuja, S., S. Mukund, L. Deng, K. Khakh, E. Chang, H. Ho, S. Shriver, C. Young, S. Lin, J.P. Johnson Jr., et al. 2015. Structural basis of Nav1.7 inhibition by an isoform-selective small-molecule antagonist. *Science.* 350:aac5464. https://doi.org/10.1126/science.aac5464

Bayrhuber, M., I. Maslennikov, W. Kwiatkowski, A. Sobol, C. Wierschem, C. Eichmann, L. Frey, and R. Riek. 2019. Nuclear magnetic resonance solution structure and functional behavior of the human proton channel. *Biochemistry.* 58:4017–4027. https://doi.org/10.1021/acs.biochem.9b00471

Berger, T.K., and E.Y. Isacoff. 2011. The pore of the voltage-gated proton channel. *Neuron.* 72:991–1000. https://doi.org/10.1016/j.neuron.2011.11.014

Bosmans, F., M.F. Martin-Eauclaire, and K.J. Swartz. 2008. Deconstructing voltage sensor function and pharmacology in sodium channels. *Nature.* 456:202–208. https://doi.org/10.1038/nature07473

Carmona, E.M., H.P. Larsson, A. Neely, O. Alvarez, R. Latorre, and C. Gonzalez. 2018. Gating charge displacement in a monomeric voltage-gated proton (H_v1) channel. *Proc. Natl. Acad. Sci. USA.* 115:9240–9245. https://doi.org/10.1073/pnas.1809705115

Chamberlin, A., F. Qiu, S. Rebolledo, Y. Wang, S.Y. Noskov, and H.P. Larsson. 2014. Hydrophobic plug functions as a gate in voltage-gated proton channels. *Proc. Natl. Acad. Sci. USA.* 111:E273–E282. https://doi.org/10.1073/pnas.1318018111

Cherny, V.V., and T.E. DeCoursey. 1999. pH-dependent inhibition of voltage-gated H(+) currents in rat alveolar epithelial cells by Zn(2+) and other divalent cations. *J. Gen. Physiol.* 114:819–838. https://doi.org/10.1085/jgp.114.6.819

De La Rosa, V., A.L. Bennett, and I.S. Ramsey. 2018. Coupling between an electrostatic network and the Zn^{2+} binding site modulates Hv1 activation. *J. Gen. Physiol.* 150:863–881. https://doi.org/10.1085/jgp.201711822

DeCoursey, T.E. 2013. Voltage-gated proton channels: molecular biology, physiology, and pathophysiology of the H(V) family. *Physiol. Rev.* 93: 599–652. https://doi.org/10.1152/physrev.00011.2012

DeCoursey, T.E., and V.V. Cherny. 1993. Potential, pH, and arachidonate gate hydrogen ion currents in human neutrophils. *Biophys. J.* 65:1590–1598. https://doi.org/10.1016/S0006-3495(93)81198-6

DeCoursey, T.E., and V.V. Cherny. 1994. Voltage-activated hydrogen ion currents. *J. Membr. Biol.* 141:203–223. https://doi.org/10.1007/BF00235130

Essmann, U., L. Perera, M.L. Berkowitz, T. Darden, H. Lee, and L.G. Pedersen. 1995. A smooth particle mesh Ewald method. *J. Chem. Phys.* 103: 8577–8593. https://doi.org/10.1063/1.470117

Feller, S.E., Y.H. Zhang, R.W. Pastor, and B.R. Brooks. 1995. Constant-pressure molecular-dynamics simulation - the Langevin piston method. *J. Chem. Phys.* 103:4613–4621. https://doi.org/10.1063/1.470648

Geragotelis, A.D., M.L. Wood, H. Göddeke, L. Hong, P.D. Webster, E.K. Wong, J.A. Freites, F. Tombola, and D.J. Tobias. 2020. Voltage-dependent structural models of the human Hv1 proton channel from long-timescale molecular dynamics simulations. *Proc. Natl. Acad. Sci. USA.* 117:13490–13498. https://doi.org/10.1073/pnas.1920943117

Gianti, E., L. Delemotte, M.L. Klein, and V. Carnevale. 2016. On the role of water density fluctuations in the inhibition of a proton channel. *Proc. Natl. Acad. Sci. USA.* 113:E8359–E8368. https://doi.org/10.1073/pnas.1609964114

Gonzalez, C., H.P. Koch, B.M. Drum, and H.P. Larsson. 2010. Strong cooperativity between subunits in voltage-gated proton channels. *Nat. Struct. Mol. Biol.* 17:51–56. https://doi.org/10.1038/nsmb.1739

Hille, B. 2001. Ion Channels of Excitable Membranes. Third edition. Sinauer Associates Inc., Sunderland, MA.

Hong, L., M.M. Pathak, I.H. Kim, D. Ta, and F. Tombola. 2013. Voltage-sensing domain of voltage-gated proton channel Hv1 shares mechanism of block with pore domains. *Neuron.* 77:274–287. https://doi.org/10.1016/j.neuron.2012.11.013

Hong, L., I.H. Kim, and F. Tombola. 2014. Molecular determinants of Hv1 proton channel inhibition by guanidine derivatives. *Proc. Natl. Acad. Sci. USA.* 111:9971–9976. https://doi.org/10.1073/pnas.1324012111

Hong, L., V. Singh, H. Wulff, and F. Tombola. 2015. Interrogation of the intersubunit interface of the open Hv1 proton channel with a probe of allosteric coupling. *Sci. Rep.* 5:14077. https://doi.org/10.1038/srep14077

Ingram, J.R., F.I. Schmidt, and H.L. Ploegh. 2018. Exploiting nanobodies' singular traits. *Annu. Rev. Immunol.* 36:695–715. https://doi.org/10.1146/annurev-immunol-042617-053327

Jorgensen, W.L., J. Chandrasekhar, J.D. Madura, R.W. Impey, and M.L. Klein. 1983. Comparison of simple potential functions for simulating liquid water. *J. Chem. Phys.* 79:926–935. https://doi.org/10.1063/1.445869

Klauda, J.B., R.M. Venable, J.A. Freites, J.W. O'Connor, D.J. Tobias, C. Mondragon-Ramirez, I. Vorobyov, A.D. MacKerell Jr., and R.W. Pastor. 2010. Update of the CHARMM all-atom additive force field for lipids: validation on six lipid types. *J. Phys. Chem. B.* 114:7830–7843. https://doi.org/10.1021/jp101759q

Koch, H.P., T. Kurokawa, Y. Okochi, M. Sasaki, Y. Okamura, and H.P. Larsson. 2008. Multimeric nature of voltage-gated proton channels. *Proc. Natl. Acad. Sci. USA.* 105:9111–9116. https://doi.org/10.1073/pnas.0801553105

Lee, S.Y., J.A. Letts, and R. Mackinnon. 2008. Dimeric subunit stoichiometry of the human voltage-dependent proton channel Hv1. *Proc. Natl. Acad. Sci. USA.* 105:7692–7695. https://doi.org/10.1073/pnas.0803277105

Liin, S.I., M. Silverå Ejneby, R. Barro-Soria, M.A. Skarsfeldt, J.E. Larsson, F. Starck Härlin, T. Parkkari, B.H. Bentzen, N. Schmitt, H.P. Larsson, and F. Elinder. 2015. Polyunsaturated fatty acid analogs act antiarrhythmically on the cardiac IKs channel. *Proc. Natl. Acad. Sci. USA.* 112:5714–5719. https://doi.org/10.1073/pnas.1503488112

Liin, S.I., J.E. Larsson, R. Barro-Soria, B.H. Bentzen, and H.P. Larsson. 2016. Fatty acid analogue N-arachidonoyl taurine restores function of I_{Ks} channels with diverse long QT mutations. *eLife.* 5:e20272. https://doi.org/10.7554/eLife.20272

Lin King, J.V., J.J. Emrick, M.J.S. Kelly, V. Herzig, G.F. King, K.F. Medzihradszky, and D. Julius. 2019. A cell-penetrating scorpion toxin enables mode-specific modulation of TRPA1 and pain. *Cell.* 178:1362–1374.e16. https://doi.org/10.1016/j.cell.2019.07.014

Lishko, P.V. 2016. Contraception: search for an ideal unisex mechanism by targeting ion channels. *Trends Biochem. Sci.* 41:816–818. https://doi.org/10.1016/j.tibs.2016.08.002

MacKerell, A.D., D. Bashford, M. Bellott, R.L. Dunbrack, J.D. Evanseck, M.J. Field, S. Fischer, J. Gao, H. Guo, S. Ha, et al. 1998. All-atom empirical potential for molecular modeling and dynamics studies of proteins. *J. Phys. Chem. B.* 102:3586–3616. https://doi.org/10.1021/jp973084f

Marcoline, F., M. Grabe, S. Nayak, T. Zahnley, G. Oster, and R. Macey. 2020. Berkeley Madonna User's Guide. Berkeley Madonna, Inc., Albany, CA. Available at: http://www.berkeleymadonna.com.

Martyna, G.J., D.J. Tobias, and M.L. Klein. 1994. Constant-pressure molecular-dynamics algorithms. *J. Chem. Phys.* 101:4177–4189. https://doi.org/10.1063/1.467468

Musset, B., S.M. Smith, S. Rajan, V.V. Cherny, S. Sujai, D. Morgan, and T.E. DeCoursey. 2010. Zinc inhibition of monomeric and dimeric proton channels suggests cooperative gating. *J. Physiol.* 588:1435–1449. https://doi.org/10.1113/jphysiol.2010.188318

Musset, B., S.M. Smith, S. Rajan, D. Morgan, V.V. Cherny, and T.E. DeCoursey. 2011. Aspartate 112 is the selectivity filter of the human voltage-gated proton channel. *Nature.* 480:273–277. https://doi.org/10.1038/nature10557

Ottosson, N.E., X. Wu, A. Nolting, U. Karlsson, P.E. Lund, K. Ruda, S. Svensson, P. Konradsson, and F. Elinder. 2015. Resin-acid derivatives as potent electrostatic openers of voltage-gated K channels and suppressors of neuronal excitability. *Sci. Rep.* 5:13278. https://doi.org/10.1038/srep13278

Phillips, J.C., R. Braun, W. Wang, J. Gumbart, E. Tajkhorshid, E. Villa, C. Chipot, R.D. Skeel, L. Kalé, and K. Schulten. 2005. Scalable molecular dynamics with NAMD. *J. Comput. Chem.* 26:1781–1802. https://doi.org/10.1002/jcc.20289

Pupo, A., and C. Gonzalez León. 2014. In pursuit of an inhibitory drug for the proton channel. *Proc. Natl. Acad. Sci. USA.* 111:9673–9674. https://doi.org/10.1073/pnas.1408808111

Ramsey, I.S., M.M. Moran, J.A. Chong, and D.E. Clapham. 2006. A voltage-gated proton-selective channel lacking the pore domain. *Nature.* 440: 1213–1216. https://doi.org/10.1038/nature04700

Ramsey, I.S., Y. Mokrab, I. Carvacho, Z.A. Sands, M.S.P. Sansom, and D.E. Clapham. 2010. An aqueous H+ permeation pathway in the voltage-gated proton channel Hv1. *Nat. Struct. Mol. Biol.* 17:869–875. https://doi.org/10.1038/nsmb.1826

Randolph, A.L., Y. Mokrab, A.L. Bennett, M.S. Sansom, and I.S. Ramsey. 2016. Proton currents constrain structural models of voltage sensor activation. *eLife.* 5:e18017. https://doi.org/10.7554/eLife.18017

Sasaki, M., M. Takagi, and Y. Okamura. 2006. A voltage sensor-domain protein is a voltage-gated proton channel. *Science.* 312:589–592. https://doi.org/10.1126/science.1122352

Seredenina, T., N. Demaurex, and K.H. Krause. 2015. Voltage-gated proton channels as novel drug targets: from NADPH oxidase regulation to sperm biology. *Antioxid. Redox Signal.* 23:490–513. https://doi.org/10.1089/ars.2013.5806

Shen, H., D. Liu, K. Wu, J. Lei, and N. Yan. 2019. Structures of human Na$_v$1.7 channel in complex with auxiliary subunits and animal toxins. *Science.* 363:1303–1308. https://doi.org/10.1126/science.aaw2493

Takeshita, K., S. Sakata, E. Yamashita, Y. Fujiwara, A. Kawanabe, T. Kurokawa, Y. Okochi, M. Matsuda, H. Narita, Y. Okamura, and A. Nakagawa. 2014. X-ray crystal structure of voltage-gated proton channel. *Nat. Struct. Mol. Biol.* 21:352–357. https://doi.org/10.1038/nsmb.2783

Tang, D., Y. Yang, Z. Xiao, J. Xu, Q. Yang, H. Dai, S. Liang, C. Tang, H. Dong, and Z. Liu. 2020. Scorpion toxin inhibits the voltage-gated proton channel using a Zn^{2+} -like long-range conformational coupling mechanism. *Br. J. Pharmacol.* 177:2351–2364. https://doi.org/10.1111/bph.14984

Tombola, F., M.H. Ulbrich, and E.Y. Isacoff. 2008. The voltage-gated proton channel Hv1 has two pores, each controlled by one voltage sensor. *Neuron.* 58:546–556. https://doi.org/10.1016/j.neuron.2008.03.026

Tombola, F., M.H. Ulbrich, S.C. Kohout, and E.Y. Isacoff. 2010. The opening of the two pores of the Hv1 voltage-gated proton channel is tuned by cooperativity. *Nat. Struct. Mol. Biol.* 17:44–50. https://doi.org/10.1038/nsmb.1738

Trott, O., and A.J. Olson. 2010. AutoDock Vina: improving the speed and accuracy of docking with a new scoring function, efficient optimization, and multithreading. *J. Comput. Chem.* 31:455–461.

Villalba-Galea, C.A. 2014. Hv1 proton channel opening is preceded by a voltage-independent transition. *Biophys. J.* 107:1564–1572. https://doi.org/10.1016/j.bpj.2014.08.017

Wulff, H., P. Christophersen, P. Colussi, K.G. Chandy, and V. Yarov-Yarovoy. 2019. Antibodies and venom peptides: new modalities for ion channels. *Nat. Rev. Drug Discov.* 18:339–357. https://doi.org/10.1038/s41573-019-0013-8

Xu, H., T. Li, A. Rohou, C.P. Arthur, F. Tzakoniati, E. Wong, A. Estevez, C. Kugel, Y. Franke, J. Chen, et al. 2019. Structural basis of Nav1.7 inhibition by a gating-modifier spider toxin. *Cell.* 176:702–715.e14. https://doi.org/10.1016/j.cell.2018.12.018

Zhao, C., L. Hong, J.D. Galpin, S. Riahi, V.T. Lim, P.D. Webster, D.J. Tobias, C.A. Ahern, and F. Tombola. 2021. HIFs: New arginine mimic inhibitors of the Hv1 channel with improved VSD–ligand interactions. *J. Gen. Physiol.* 153. https://doi.org/10.1085/jgp.202012832
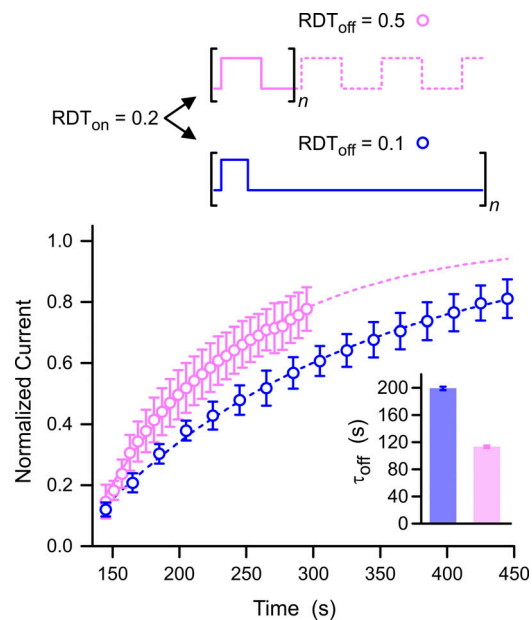
Supplemental material

Figure S1. **Effect of depolarization frequency on recovery from HIF-mediated inhibition.** Time courses of recovery from inhibition of Hv1 WT measured with the two indicated voltage protocols (V_d = +120 mV, V_r = −40 mV). In both cases, 100 μM HIF was perfused into the bath until current inhibition reached ~90%. The current was monitored using a protocol with RDT_{on} = 0.2 (t_d = 3 s, t_r = 12 s). The inhibitor was then washed out and the recovery from inhibition monitored under a protocol with RDT_{off} = 0.5 (t_d = t_r = 3 s) or under a protocol with RDT_{off} = 0.1 (t_d = 2 s, t_r = 18 s). Points are averages from six independent measurements; error bars are SEM. Time courses were fitted with a single-exponential function. Time constants from fits are shown in the bar graph (± SE). The current recovers faster when the relative time spent in the O state is longer (RDT_{off} = 0.5, pink).
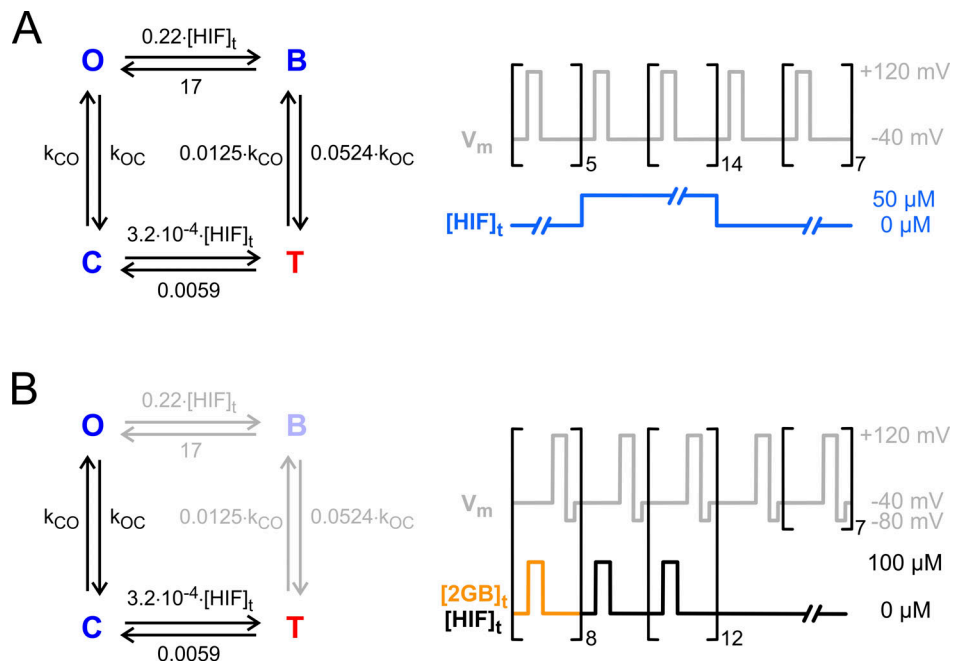
Figure S2. **Kinetic modeling of HIF-mediated Hv1 inhibition (model S).** Kinetic constants for transitions C → T and O → B are in $\mu M^{-1} s^{-1}$; for the other transitions, they are in s^{-1}. **(A)** Parameters and protocols used to generate the time course of inhibition and current traces in Fig. 2 C. $[HIF]_t = 50$ µM for both the C → T and the O → B transitions when the inhibitor is continuously perfused in the bath (sweeps 6–20). **(B)** Parameters and protocols used to generate the time course of inhibition in Fig. 2 F. 2GBI or HIF are perfused into the bath only when the channel is closed. When the inhibitor is present, $[HIF]_t = 100$ µM for the C → T transition and $[HIF]_t = 0$ µM for the O → B transition. 2GBI was present in the first eight sweeps; HIF was present in sweeps 9–21. Sweep length was 15 s in both A and B, with a depolarization step of 3 s. The duration of the inhibitor application in protocol B was 10% longer than the nominal value (3 s) to account for the noninstantaneous changes in inhibitor concentration attainable experimentally. k_{CO} was 0.884 s^{-1} at +120 mV, and $2.27 \cdot 10^{-4} s^{-1}$ at -40 mV. k_{OC} was 0.0465 s^{-1} at +120 mV and 2.27 s^{-1} at −40 mV. To simulate accelerated channel closure at −80 mV in protocol B, the value of k_{OC} was set to 10.2 s^{-1} during the hyperpolarization step, while k_{CO} was kept at $2.27 \cdot 10^{-4} s^{-1}$. The transitions connecting the T and B states had the same voltage dependence as the transitions connecting the C and O states, but they were slowed down by the indicated factors. Current was calculated as I = $G_{max} \cdot O \cdot V_m$, with $G_{max} = 8.33$ pA/mV.
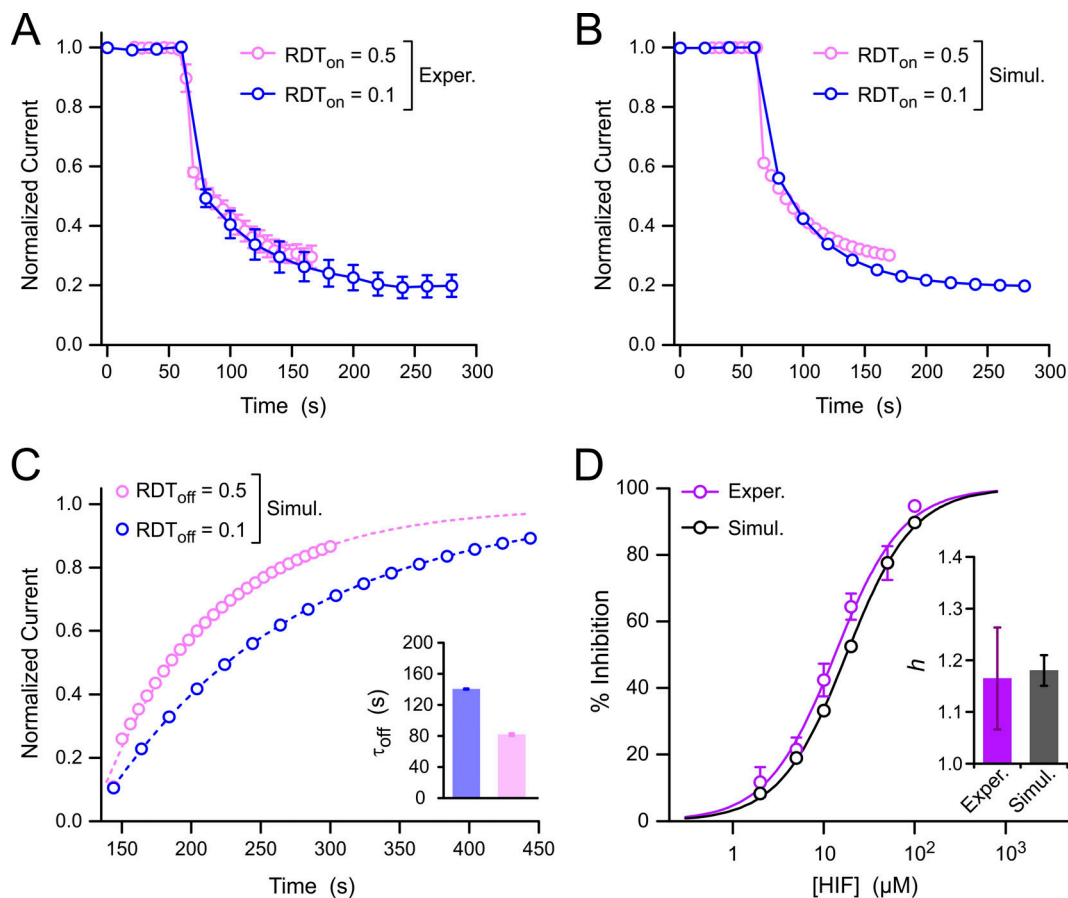
Figure S3. **Comparisons between experimental and simulated data using model S. (A and B)** Experimental and simulated time courses of HIF-mediated inhibition of Hv1 WT as a function of RDT_{on}. Experimental data are the same as in Fig. 1 B. The recovery from inhibition was omitted for clarity. τ_{slow} values as a function of RDT_{on} are reported in Fig. 1 C; $\tau_{slow, RDTon = 0.1}/\tau_{slow, RDTon = 0.5}$ = 1.15 ± 0.20. Time courses of inhibition reported in B were generated with the four-state model of Fig. S2 A. The simulated data were then fitted with a double-exponential function providing $\tau_{slow, RDTon = 0.1}/\tau_{slow, RDTon = 0.5}$ = 1.03 ± 0.05. Hence, τ_{slow} is only weakly affected by differences in RDT_{on} in both experiments and simulations. **(C)** Simulated time courses of recovery from inhibition of Hv1 WT as a function of RDT_{off}. Conditions and protocols were as in Fig. S1. Time courses were fitted with a single-exponential function. Time constants from fits are shown in the bar graph (± SE). Simulated currents recover faster when the relative depolarization time increases, as observed experimentally (Fig. S1). **(D)** Concentration dependence of HIF-mediated Hv1 inhibition simulated with the four-state model of Fig. S2 A shown in black compared with the experimental concentration dependence from Zhao et al. (2021) shown in purple. Each experimental data point represents the mean of three to five independent measurements ± SD. Simulated and experimental data points were fitted with the Hill equation (Eq. 4). The resulting Hill coefficients (h) are compared in the bar graph. Error bars are SE. Simulated half maximal inhibitory concentration (IC_{50}) was 17.7 ± 0.4 µM. Experimental IC_{50} was 13.3 ± 1.0 µM (Zhao et al., 2021). The simulated data were generated by applying the same protocols used in the experiments. So, we assume that $h > 1$ could be due, at least in part, to some imperfect experimental conditions (e.g., not reaching true steady state of inhibition at all concentrations; see Discussion). Exper., experiment; Simul., simulation.
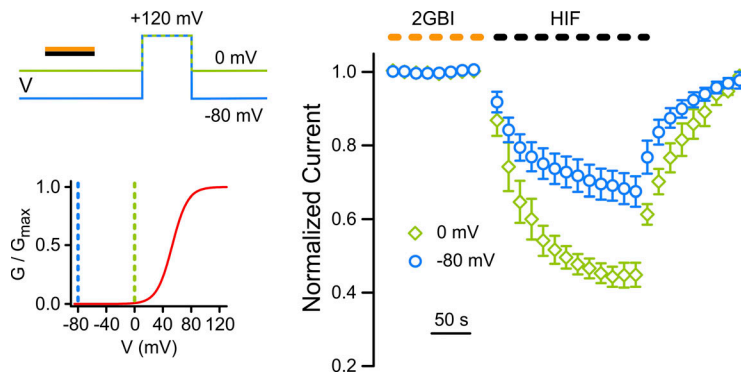
Figure S4. **Effect of voltage on HIF apparent binding to C state.** Time courses of Hv1 inhibition by 2GBI and HIF and recovery from inhibition. 100 µM 2GBI (yellow) or HIF (black) were transiently perfused when holding the membrane at 0 mV (green) or –80 mV (blue). Sweep length was 15 s with a depolarization step of 3 s. Conditions were as in Fig. S2 B. The channel is expected to be in a deeper resting state at –80 mV than at 0 mV; see G-V curve (red) in inset. Current was measured with a depolarization step at +120 mV delivered after the inhibitor was removed from the solution. 2GBI failed to produce any inhibition, consistent with its inability to bind the channel in the closed state. HIF produced inhibition at both voltages, and the extent of inhibition was larger at 0 mV compared with –80 mV. Points are averages from at least five independent measurements; error bars are SEM.
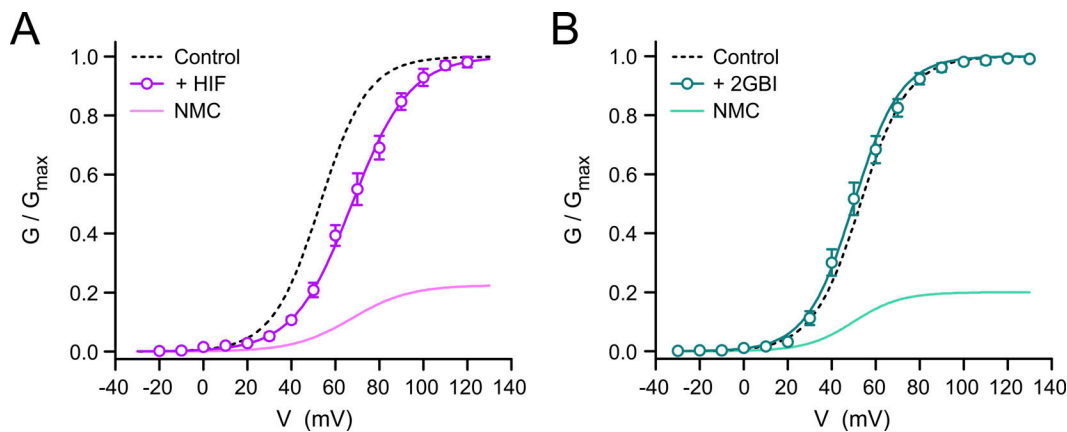

Figure S5. **Effect of HIF on the conductance versus voltage relationship of Hv1 WT. (A)** G-V curves for Hv1 WT in the presence of 50 µM HIF (circles) and in the absence of the inhibitor (dashed line). Points are averages from at least five independent measurements ± SEM ($V_{1/2}$ = 68 ± 2 mV, slope = 13 ± 1 with HIF; $V_{1/2}$ = 53 ± 3 mV, slope = 11 ± 1 without HIF). NMC is the G-V in the presence of the inhibitor normalized to the control maximal conductance (no inhibitor). **(B)** G-V curves for Hv1 WT in the presence of 200 µM 2GBI (circles) and in the absence of the inhibitor (dashed line). NMC is the G-V in the presence of the inhibitor normalized to the control maximal conductance (no inhibitor). Data for 2GBI are from Hong et al. (2013) and reported here for comparison. All G-Vs were measured at pH_i = pH_o = 6.0. The concentrations of HIF and 2GBI were chosen based on their ability to reduce G_{max} to a similar extent.
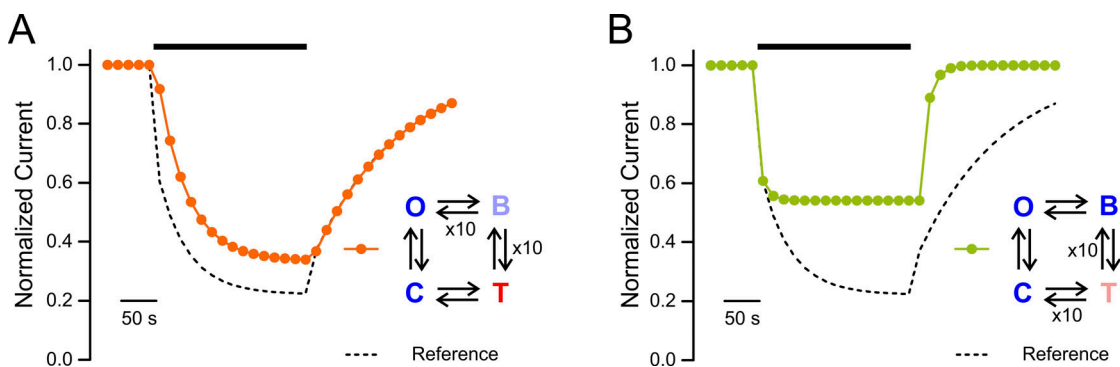

Figure S6. **Simulations of the time course of HIF-mediated inhibition of Hv1 channels with destabilized B or T states.** Simulations were performed with model S shown in Fig. 2. Rate constants were as in Fig. S2 A (reference), with the exception of the indicated transitions. **(A)** Destabilization of the B state was simulated by a 10-fold acceleration of HIF unbinding from the B state (10× k_{OB}) and a 10-fold acceleration of the B → T transition (10× k_{BT}). The result is the disappearance of the fast component of the time course of inhibition (τ_{fast} cannot be precisely derived from the double-exponential fit). **(B)** Destabilization of the T state was simulated by a 10-fold acceleration of HIF unbinding from the T state (10× k_{CT}) and a 10-fold acceleration of the T → B transition (10× k_{TB}). The result is the disappearance of the slow component of the time course of inhibition (τ_{slow} cannot be precisely derived from the double-exponential fit).

A

O $\xrightleftharpoons[0.532]{14.4 \cdot [HIF]_t}$ B

$k_{CO} \| k_{OC}$ $0.166 \cdot k_{CO}$ $3.33 \cdot 10^{-4} \cdot k_{OC}$

C $\xrightleftharpoons[0.0059]{3.2 \cdot 10^{-4} \cdot [HIF]_t}$ T

B

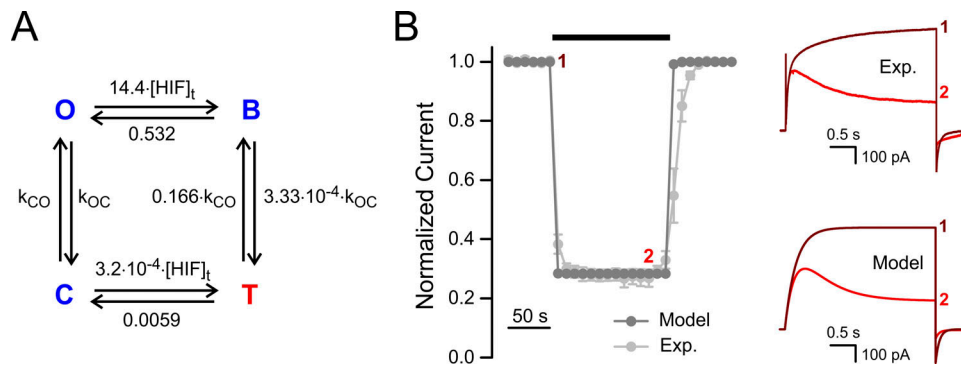Figure S7. **Simulations of the time course of HIF-mediated inhibition of Hv1 F150A. (A)** Parameters used to simulate inhibition of Hv1 F150A by 0.1 μM HIF with model S. Kinetic constants for the C → T and O → B transitions are in μM^{-1}s^{-1}. They are in s^{-1} for the other transitions. F150A causes faster channel gating compared with Hv1 WT (Hong et al., 2013). Accordingly, k_{CO} was 4.42 s^{-1} at +120 mV and 2.27 · 10^{-4} s^{-1} at −40 mV; k_{OC} was 0.233 s^{-1} at +120 mV and 13.6 s^{-1} at −40 mV. **(B)** Comparison between simulated (dark gray) and experimental time course of inhibition (light gray). The experimental data are the same as in Fig. 3 C. Representative current traces on the right correspond to the indicated points, before (1) or after (2) perfusion of HIF. In the presence of the inhibitor, the current first increases upon depolarization and then decreases. The average ratio between the peak current and the current at the end of the depolarization step in the presence of the inhibitor was 2.5 ± 0.5 (SEM, n = 5) to be compared with 2.1 from the simulation. The biphasic shape is expected for open channel block. We propose that the reason why this behavior is observed in the mutant channel but not in the WT is that the activation process is rate limiting in the WT (channel activation much slower than channel block) as previously observed with 2GBI (Hong et al., 2013). In the simulation, the current was calculated as I = G_{max} · O · V_m, with G_{max} = 5.46 pA/mV. Exp., experiment.
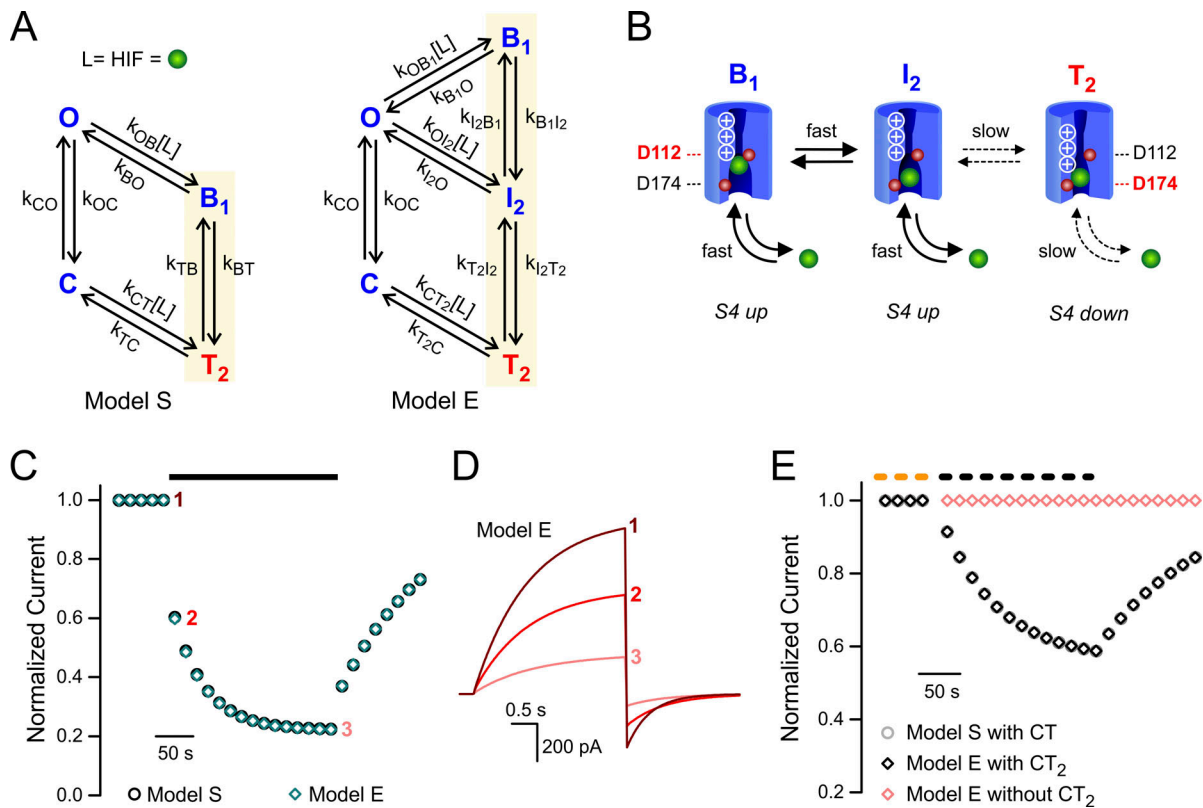
Figure S8. **Extended model E compared with model S. (A)** Kinetic schemes of model S and model E highlighting the expansion of the $B_1 \leftrightarrow T_2$ transition (same as B $\leftrightarrow$ T in Fig. 2 and Fig. S2) to the $B_1 \leftrightarrow I_2 \leftrightarrow T_2$ transitions. Rate constants k_{CO} and k_{OC} are the same in the two models (as in Fig. S2 A) and have the same values as k_{TC} and k_{CT} of model S, respectively. The other parameters for model E are as follows: $k_{OB1} = 0.19\ \mu M^{-1}s^{-1}$, $k_{B1O} = 19\ s^{-1}$, $k_{OI2} = 0.10\ \mu M^{-1}s^{-1}$, $k_{I2O} = 30.9\ s^{-1}$, $k_{B1I2} = 10\ s^{-1}$, $k_{I2B1} = 30.9\ s^{-1}$, $k_{CT2}, = 3.2 \cdot 10^{-4}\ \mu M^{-1}s^{-1}$, $k_{T2C} = 0.0059\ s^{-1}$, $k_{I2T2} = 0.21 \cdot k_{OC}$, and $k_{T2I2} = 0.0125 \cdot k_{CO}$. **(B)** Schematics of B_1, I_2, and T_2. The first two states correspond to an open VSD conformation and the third to a closed VSD conformation. When the VSD is open (S4 up), HIF is assumed to have access to both site 1 and site 2 and to be able to quickly move from one site to the other ($B_1 \leftrightarrow I_2$ transition). When the VSD is closed (S4 down), HIF is assumed to have access to site 2 only. VSD activation is slowed down by the interaction with HIF in both models. **(C)** Time courses of HIF-mediated Hv1 inhibition and recovery simulated with model E and model S. Black bar indicates the presence of 50 µM HIF in the bath compartment. **(D)** Current traces generated by model E (G_{max} as in Fig. S2) at the time points indicated in C. **(E)** Time courses of channel inhibition under pulsed delivery of HIF (protocol in Fig. 2 E) simulated by model E and model S. Yellow and black dashed lines indicate recurring transient exposure to 100 µM 2GBI or HIF, respectively. Black and red diamonds indicate normalized current predicted in the presence and absence of the C $\leftrightarrow$ T$_2$ transition, respectively.
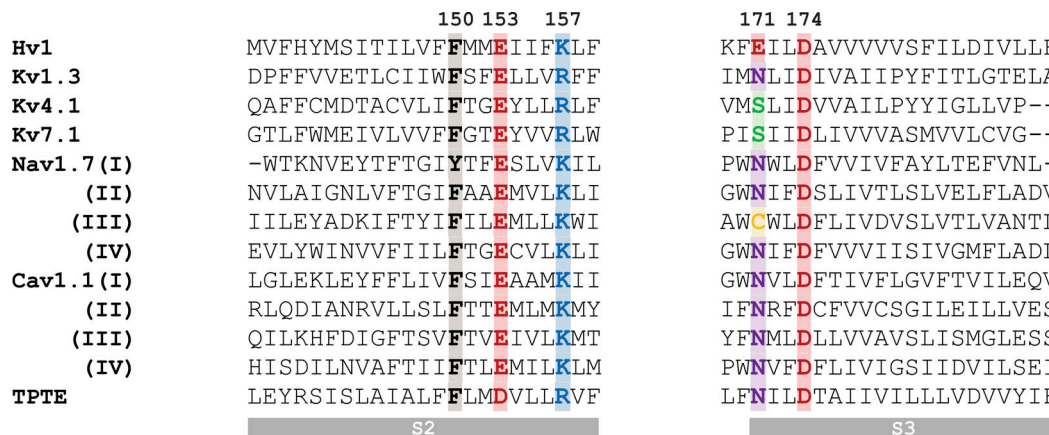

Figure S9. **Sequence alignment of S2 and S3 segments from representative human VSD-containing proteins.** Included in the comparison are three different potassium channels (Kv1.3/KCNA3, Kv4.1/KCND1, Kv7.1/KCNQ1), the four domains (I–IV) of the sodium channel Nav1.7/SCN9A and calcium channel Cav1.1/CACNA1S, and the VSD of TPTE, a human homologue of the CiVSP phosphatase. Highlighted are positions corresponding to F150 and residues contributing to the intracellular electrostatic network in the VSD intracellular vestibule. VSD ligands that bind in proximity of the conserved D174 could alter its interactions with other elements of the network, including the positively charged residues in S4.